This article has been accepted for publication and undergone full peer review but has not been through the copyediting, typesetting, pagination and proofreading process, which may lead to differences between this version and the Version of Record. Please cite this article as doi: 10.1111/GCB.15905

PRIMARY RESEARCH ARTICLE

Journal Section

The CO_2 record at the Amazon Tall Tower Observatory: a new opportunity to study processes on seasonal and inter-annual scales

Santiago Botía[1*] | Shujiro Komiya[2] | Julia Marshall[3] | Thomas Koch[1] | Michał Gałkowski[1,10] | Jost Lavric[2] | Eliane Gomes-Alves[2] | David Walter[4] | Gilberto Fisch[5] | Davieliton M. Pinho[6] | Bruce W. Nelson[6] | Giordane Martins[6] | Ingrid T. Luijkx[7] | Gerbrand Koren[7] | Liesbeth Florentie[7] | Alessandro Carioca de Araújo[11] | Marta Sá[12] | Meinrat O. Andreae[9,13] | Martin Heimann[1,14] | Wouter Peters[7,8] | Christoph Gerbig[1]

[1]-Biogeochemical Signals Department, Max Planck Institute for Biogeochemistry, 07745 Jena, Germany

[2]-Biogeochemical Processes Department, Max Planck Institute for Biogeochemistry, 07745 Jena, Germany

[3]-Deutsches Zentrum für Luft- und Raumfahrt (DLR), Institut für Physik der Atmosphäre, Oberpfaffenhofen, Germany

[4]-Multiphase Chemistry Department, Max Planck Institute for Chemistry, 55128 Mainz, Germany

[5]-Instituto de Aeronautica e Espaço (IAE), Departamento de Ciência e Tecnologia Aeroespacial (DCTA), São José dos Campos, Brazil

[6]-Environmental Dynamics Department, Brazil's National Institute for Amazon Research – INPA, Av. André Araújo, 2936, Manaus, Brazil

[7]-Meteorology and Air Quality Department, Wageningen University and Research Center, 6708PB Wageningen, The Netherlands

[8]-Groningen University, Energy and Sustainability Research Institute Groningen, 9747 AG Groningen, The Netherlands

[9]-Biogeochemistry Department, Max Planck Institute for Chemistry, 55128 Mainz, Germany

[10]-Faculty of Physics and Applied Computer Science, AGH University of Science and Technology, Kraków, Poland

[11]-Empresa Brasileira de Pesquisa Agropecuária (EMBRAPA), Trav. Dr. Enéas Pinheiro, Belém, PA, Brazil

[12]-Instituto Nacional de Pesquisas da Amazônia (INPA), Av. André Araújo 2936, Manaus, AM, Brazil

[13]-Scripps Institution of Oceanography, University of California San Diego, La Jolla, CA 92093, USA

[14]-Institute for Atmospheric and Earth System Research (INAR) / Physics, FI-00014 University of Helsinki, Finland

1 | ABSTRACT

High quality atmospheric CO_2 measurements are sparse in Amazonia, but can provide critical insights into the spatial and temporal variability of sources and sinks of CO_2. In this study we present the first six years (2014-2019) of continuous, high-precision measurements of atmospheric CO_2 at the Amazon Tall Tower Observatory (ATTO, 2.1°S, 58.9°W). After subtracting the simulated background concentrations from our observational record, we define a CO_2 regional signal ($\Delta CO_{2_{obs}}$) that has a marked seasonal cycle with an amplitude of about 4 ppm. At both seasonal and inter-annual scales we find differences in phase between $\Delta CO_{2_{obs}}$ and the local eddy covariance net ecosystem exchange (EC-NEE), which is interpreted as an indicator of a decoupling between local and non-local drivers of $\Delta CO_{2_{obs}}$. In addition, we present how the 2015/2016 El Niño-induced drought was captured by our atmospheric record as a positive 2σ anomaly in both the wet and dry season of 2016. Furthermore, we analyzed the observed seasonal cycle and inter-annual variability of $\Delta CO_{2_{obs}}$ together with net ecosystem exchange (NEE) using a suite of modeled flux products representing biospheric and aquatic CO_2 exchange. We use both non-optimized and optimized (i.e., resulting from atmospheric inverse modeling) NEE fluxes as input in an atmospheric transport model (STILT). The observed shape and amplitude of the seasonal cycle was captured neither by the simulations using the optimized fluxes nor by those using the diagnostic Vegetation and Photosynthesis Respiration Model (VPRM). We show that including the contribution of CO_2 from river evasion improves the simulated shape (not the magnitude) of the seasonal cycle when using a data-driven non-optimized NEE product (FLUXCOM). The simulated contribution from river evasion was found to be 25% of the seasonal cycle amplitude. Our study demonstrates the importance of the ATTO record to better understand the Amazon carbon cycle at various spatial and temporal scales.

2 | INTRODUCTION

Amazonia covers approximately one third of South America, and 70-80% of its area is rain forest (Goulding et al., 2003). This vast expanse of forest stores approximately 85-130 Pg of carbon in above- and below-ground biomass, making it one of the largest carbon pools on the globe (Malhi et al., 2006; Saatchi et al., 2007; Feldpausch et al., 2012; Baccini et al., 2012). Hence, Amazonia plays a fundamental role in the global carbon cycle not only by storing massive amounts of carbon, but also by acting as an immense "biogeochemical reactor" (Andreae, 2001). The exchange between the biosphere and the atmosphere occurs mainly through CO_2 exchange (Friedlingstein et al., 2020). Therefore, atmospheric mole fraction measurements of CO_2 can provide information about this exchange, as they integrate signals from the underlying ecosystem over large scales. Atmospheric CO_2 can thus be used to study the spatial and temporal variability of the dominant sources and sinks of carbon, which in the central part of Amazonia are mainly photosynthesis and respiration (Malhi et al., 2015).

The principal threats to Amazonia are forest degradation and deforestation, agricultural expansion and climate variability (Davidson et al., 2012; Mitchard, 2018). Deforestation was recently shown to cause disturbed rainfall patterns upwind and downwind of the cleared areas during the dry season in Amazonia (Khanna et al., 2017). In addition, deforestation and agricultural expansion are directly associated with biomass burning (van der Werf et al., 2010; Barlow et al., 2020), which in turn can be intensified by severe drought (Gatti et al., 2014; van der Laan-Luijkx et al., 2015; Marengo and Espinoza, 2016; Aragão et al., 2018). Extremes in the hydrological cycle include both droughts and flooding, which can be enhanced by large-scale events, such as those occuring during the extreme phases of the El Niño Southern Oscillation (ENSO) cycle (Marengo and Espinoza, 2016; van Schaik et al., 2018; Malhi et al., 2018). Variability in the hydrological cycle in the Amazon has increased over the last two decades (Gloor et al.,

2015), with more frequent extreme events. At the same time, a significant increase in the length of the dry season in southern Amazonia has been reported by Fu et al. (2013). Gloor et al. (2012) suggest that even though biospheric carbon uptake currently compensates for deforestation and fossil fuel emissions in South America, the continent could become a net source of carbon over the next decades, as projected by up-scaled plot level studies (Brienen et al., 2015; Hubau et al., 2020). Therefore, observational ground sites (such as ATTO) that can provide ground truth data for evaluating predictions are critical to improve our understanding of the carbon cycle in Amazonia.

The ecosystem net carbon exchange can be estimated using either a top-down or a bottom-up approach. Atmospheric inversions (i.e., the top-down approach) use measurements of atmospheric CO_2 mole fractions to optimize a prior estimate of net ecosystem exchange (NEE) fluxes at global (Gurney et al., 2002; Rödenbeck et al., 2003; van der Laan-Luijkx et al., 2017) and continental scales (Gerbig et al., 2003; Peters et al., 2007; Schuh et al., 2010; Shiga et al., 2018; Kountouris et al., 2018; Hu et al., 2019). This method is highly dependent on well-calibrated accurate measurements, their spatial density and representativeness (Gerbig et al., 2009). Typically, fluxes in regions with few measurements will be estimated with high uncertainties that will lead to limited understanding of spatial and temporal patterns (Gurney et al., 2002; Peylin et al., 2013; van der Laan-Luijkx et al., 2015; Thompson et al., 2016). Global inverse models have been found to be under-constrained (Gurney et al., 2002; Gaubert et al., 2019) and to a large extent hampered by model uncertainties and insufficient measurements in the Amazon region (Molina et al., 2015). Moreover, the density of remotely-sensed satellite columns over the region, characterized by deep convection, is highly reduced due to persistent cloud cover (Liu et al., 2017; Basu et al., 2018). The combination of these factors makes it difficult to constrain the seasonal and inter-annual variability of carbon exchange in Amazonia (Molina et al., 2015). The aircraft network of CO_2 profiles (Gatti et al., 2014) at several sites across Amazonia represents an important advance in the regional effort to improve the observational constraint for inverse modeling studies (van der Laan-Luijkx et al., 2015; Alden et al., 2016), yet identifying the relevant processes responsible for inter-annual and seasonal changes remains challenging.

Process-based biosphere models (representing the bottom-up approach) provide an alternative to constrain carbon exchange accross a wide range of ecosystems (Sitch et al., 2015). However, the inability to reproduce the cycle of gross primary productivity (GPP), which influences the amplitude and phase of NEE at equatorial sites in Amazonia is one of the important limitations of biosphere models (Restrepo-Coupe et al., 2017). Others include e.g. CO_2 fertilization effect (Fleischer et al., 2019) and ecosystem respiration (Carvalhais et al., 2014). While process-based model simulations show a decline in dry-season GPP at equatorial sites, presumably based on an incorrect assumption of water-limitation, observations typically suggest that GPP increases during the dry season (Huete et al., 2006; Myneni et al., 2007; Brando et al., 2010; Restrepo-Coupe et al., 2013; Borchert et al., 2015; Wu et al., 2016; Green et al., 2020). This discrepancy may be explained by the lack of leaf phenology in model formulations (Gonçalves et al., 2020). Chen et al. (2020) recently corroborated this by implementing this mechanism in the biosphere model ORCHIDEE, yet it is still missing in other biosphere models.

The evaluation of model-based biosphere-atmosphere flux estimates is generally performed by comparing simulated fluxes with in-situ flux measurements. Eddy-flux and plot-level studies serve such purposes and are valuable for understanding processes and underlying drivers of carbon exchange (Verbeeck et al., 2011; von Randow et al., 2013; Restrepo-Coupe et al., 2017). An alternative approach to evaluate both biosphere models and inverse modeling results is to use surface fluxes as an input in atmospheric transport models, and compare simulated and observed mole fractions at independent measurement sites. This method has the advantage of attributing the observed CO_2 regional signal to a larger spatial area, as compared to local eddy-flux spatial coverage, especially when atmospheric CO_2 is measured at a tall tower (Gloor et al., 2001). However, atmospheric transport errors can add additional biases that should be considered when interpreting patterns at different temporal scales (Gerbig et al., 2008). This leads to

different models presenting widely varying perspectives on the processes influencing Amazonia's carbon budget, with most of them being poorly constrained by actual observations.

All things considered, accurate atmospheric CO_2 measurements at high temporal resolution can provide valuable information about the spatial and temporal variability of sources and sinks of CO_2. In this work, we present six years of observations from the Amazon Tall Tower Observatory (ATTO) in central Amazonia, and demonstrate how they can be used to increase our process understanding by identifying the main sources of variability at seasonal and inter-annual scales. Furthermore, we use the CO_2 measurements to evaluate state-of-the-art top-down as well as bottom-up NEE products using an atmospheric transport model. A highlight of this study is that we use three different estimates of NEE fluxes generated using CarbonTracker South America (an inverse modeling system) (van der Laan-Luijkx et al., 2015), the Vegetation Photosynthesis and Respiration diagnostic model (VPRM) (Mahadevan et al., 2008), and a statistically upscaled NEE product (Bodesheim et al., 2018) (FLUXCOM). With such a diverse dataset of NEE fluxes, we cover the inherent variability of different model formulations. We also evaluate the capability of an inversion system, using different data streams for optimization, to constrain the variability of atmospheric CO_2 at ATTO. Thus, we provide valuable insights that will serve not only to better understand the processes that control atmospheric CO_2 at ATTO, but also to evaluate biosphere flux models from an atmospheric perspective.

3 | DATA AND METHODS

3.1 | Site description

The Amazon Tall Tower Observatory (ATTO) site (2.14°S, 58.99°W, see Figure 6) has been described extensively in Andreae et al. (2015). In this paper, we present aspects considered important for our study. ATTO is located in the Uatumã Sustainable Development Reserve (USDR) in central Amazonia, 150 km northeast of the closest large city, Manaus. The main infrastructure and research facilities were built in the dense upland forest (terra fime, at 130 m a.s.l.), where the highest vegetation is found. The canopy height at the tower location is around 37 m, however the average tree height on the terra firme forest plateau is 20.7 ± 0.4 m (Andreae et al., 2015).

The local precipitation regime shows a distinct seasonality (see Figure S1 left panel), and agrees very well (r=0.8, p-value<0.01) with the Multi-Satellite Precipitation Analysis from the Tropical Rainfall Measuring Mission (TRMM 3B42-daily at a resolution of 0.25 deg, obtained from: `https://disc.gsfc.nasa.gov/datasets/TRMM_3B42_Daily_7/summary`) (Huffman et al., 2016) sampled at the grid cell closest to ATTO (2.12°S, 58.87°W). However the local measurements show a lower mean annual precipitation (MAP) than the climatological average obtained using the TRMM dataset (1934.1 mm yr^{-1} vs 2382.2 mm yr^{-1}). The monthly and annual mean biases of the TRMM estimate with respect to the local measurements is +40 mm and +489 mm, respectively. The local time series is based on an 8-year record (2012-2019), and thus the seasonal average is highly affected by the 2015/2016 El Niño drought. Therefore, we consider the longer TRMM dataset (ATTO-TRMM 1998-2019 in Table 1) to be more reliable as a climatology. Thus, we use the ATTO-TRMM (1998-2019) record as a reference; the dry season length (DSL) is 3 months with a mean dry season precipitation of 63.3 mm $month^{-1}$. The annual minimum average precipitation (MiAP) is 45.1 mm $month^{-1}$. A comparison of these values between the local record and the TRMM dataset is shown in Table 1. For this study we have defined the climatological dry season as the months whose seasonal median is lower than 100 mm (July to October). For the wet season we selected the months whose 25th percentile was clearly above 200 mm (February to June), see Figure S1 right panel for details.

TABLE 1 Mean annual precipitation (MAP), mean dry season precipitation (DSP), mean dry season length (DSL) and annual minimum average precipitation (MiAP) at ATTO using the local precipitation measurements (2012-2019) and data from the tropical rainfall measuring mission (TRMM) from 1998-2019 (Huffman et al., 2016). For comparison we show the same values reported by Restrepo-Coupe et al. (2017) for the research station (K34) for the period 1998-2014.

Site	Lat (°)	Lon(°)	MAP (mm yr^{-1})	DSP (mm $month^{-1}$)	DSL (months)	MiAP (mm $month^{-1}$)
ATTO-Local (2012-2019)	-2.14	-58.99	1934.1	53.2	3.8	25.3
ATTO-TRMM (2012-2019)	-2.12	-58.87	2422.6	63.3	2.8	42.2
ATTO-TRMM (1998-2019)	-2.12	-58.87	2382.2	63.3	3	45.1
K34-TRMM (1998-2014)	-2.61	-60.21	2672.6	99.7	1-2	99.7

3.2 | Atmospheric mole fraction measurements

The continuous measurement system was installed in March 2012 at the 81 m walk-up tower at ATTO and has been described in Andreae et al. (2015) and Botía et al. (2020). Here we highlight the features relevant for this study. The atmospheric mixing ratio data presented here were collected with two cavity ring-down-based analyzers (Picarro Inc., USA), a G1301 and a G1302 measuring CH_4/CO_2 and CO_2/CO, respectively. Both analyzers provide CO_2 data at a 15-minute resolution calibrated on the World Meteorological Organization (WMO) CO_2 X2007 scale. These data were subsequently averaged to half-hourly data. The overall accuracy of both analyzers, including the uncertainties of the water vapor correction, are estimated to be 0.09 ppm CO_2 (1 ppm = 1 μmol mol^{-1} of dry air). The analyzers measure the air from five lines connected to inlets located at 79, 53, 38, 24 and 4 m above ground. Downstream of each sampling line, a stainless steel sphere (8 liters volume) acts as a buffer volume. By mixing the sampled air, these buffers integrate the atmospheric signal, allowing a continuous, near-concurrent measurement from all heights (Winderlich et al., 2010). The time series presented here is based on only daytime dry air mole fractions (i.e., 13:00 to 17:00 local time (LT)), representative of well-mixed convective conditions. In order to maximize the data coverage, we use observations from both instruments whenever they are available, with the mean calculated for the periods when both were operational simultaneously. The mean bias between the datasets at half-hourly resolution was estimated to be 0.02 ppm CO_2. The data presented here are available upon request at https://attodata.org (last access: 25 January 2021).

3.3 | Phenology measurements and leaf area index age classes

Upper canopy leaf phenology is monitored with a RGB Stardot Netcam model XL 3MP (2048×2536 pixels) mounted on the top of the 81 m tower. For an in-depth description of the camera set-up, radiometric calibration and detection of phenostages, we refer the reader to Lopes et al. (2016). We used only pictures obtained in the morning (i.e., no backlit crowns), under cloudy sky or under the shadow of a cloud, providing a spatially even and temporally consistent illumination of the irregular canopy surface. For each crown (n=194), we were able to detect abrupt increase in greenness (i.e., leaf flush) or abrupt green-down (i.e., leaf abscission). By counting the number of individual trees per month for each category (flush or abscission), we built a monthly time series for the period between July 2013 and November 2018. From the trees that the camera sees, 69% (n=134) have clear flushing and abscission patterns, and from these the time series was built.

Using the number of days after each individual flushing event, we determined leaf age classes and attributed a fraction of the upper canopy crowns to an age class at monthly intervals. As in Wu et al. (2016), we defined the

following leaf age classes: i) young leaves (0-2 months), ii) mature leaves (2-6 months), and iii) old leaves (>6 months). Next, we partitioned the age classes into classes of leaf area index (LAI) (i.e., young, mature, and old LAI) by normalizing each leaf age class with the total LAI measured at ATTO. We used a constant LAI of 5.32 m^2 m^{-2} for all months, as the variability of this number throughout the year was not statistically significant (unpublished results). For the normalization we took into account the total number of trees in the camera frame (n=194), assuming that the 30% that does not have clear flushing patterns are part of the old age class. For more details on the methods and assumptions for the separation of LAI into leaf age classes, see Wu et al. (2016). LAI was measured using two LAI-2200 PCA sensors (LI-COR Inc., Lincoln, NE, USA) recording simultaneous readings above and within the canopy. The sensor above the canopy (the reference) was installed on the 80 m tower (approximately 50 meters above top canopy). All measurements were performed under diffuse light conditions. The within-canopy measurements were carried out using 40 cm supports (sampling points) on the ground. The spatial sampling design was a square grid with 42 sampling points (21x2 and 80m between points). We carried out monthly campaigns from March 2016 to March 2019. The flushing and abscission data (http://doi.org/10.17871/atto.223.7.840) together with the raw LAI age classes (http://doi.org/10.17871/atto.230.4.842) are available upon request request at https://attodata.org.

3.4 | Eddy covariance measurements

In this study, we use eddy covariance (EC) measurements from 2014 to 2019. They were done using a 3-D sonic anemometer (CSAT3, Campbell Scientific Inc., Logan, USA) and an open-path infrared gas analyser (LI7500, Li-COR Inc., Lincoln, USA), both installed at the top of the 81 m tower, approximately 40 m above the local canopy top. Half-hourly EC-sensible heat (EC-H), EC-latent heat (EC-LE), and EC-CO_2 fluxes were calculated by using EddyPro software (Li-COR Inc., Lincoln, USA). Raw time series data were de-spiked and screened according to Vickers and Mahrt (1997), and data quality control on half-hourly EC-H/LE/CO_2 fluxes was carried out following the method of Mauder and Foken (2004). EC flux data meeting the highest quality criteria (flags 0 and 1) for H, LE and CO_2 and from the EC-favourable wind direction ([-90° : +90°] sector) were selected for further analysis. The raw eddy-flux data are available upon request at https://attodata.org (last access: 25 January 2021).

Net ecosystem exchange (EC-NEE) was calculated as the sum of the half-hourly EC-CO_2 flux and storage CO_2 flux. The storage flux was obtained using the 5-inlet CO_2 mole fraction profile measurements at the 81 m tower (cf. section 3.2) following the calculation procedure of Winderlich et al. (2014). When the profiles were missing measurements from one or two heights, the storage flux was obtained from 3 or 4 inlets that included both the 4 m and 79 m heights, this occurred only 2.42% of the time over the six years. In cases where only half-hourly EC-CO_2 flux data were available, missing CO_2 storage fluxes were gap-filled with mean diurnal variations over ± 14-day periods as performed by the REddyProc package (Wutzler et al., 2018). In addition, negative EC-NEE data during nighttime periods (defined as 18:00 to 6:00 with global radiation (R_g) < 20 W m^{-2}) were removed. In cases where nighttime R_g data were not available, we discarded negative EC-NEE data between 19:00 and 5:00.

A distribution of friction velocity (u*) thresholds (5th, 50th and 95th percentiles) in each year was estimated according to Papale et al. (2006) using REddyProc. For this study, we used the yearly median (50th percentile) u* values as representative for our site (see Table S1). Our u* values are lower than those from previous studies due to the higher measurement height (81 m), we refer the reader to Table S2 for a comparison of u* values in other sites in Amazonia. After the u* filtering, 20.4 % of EC-NEE data remained. The effect of having more or less data due to a larger or lower u* threshold does not affect the seasonal cycle of neither EC-NEE, GPP nor R_{eco}, this is shown in Figure S2. The gap-filling of the EC-NEE data was performed using REddyProc and then negative gap-filled nighttime EC-NEE data were screened out. The missing nighttime EC-NEE data were gap-filled by a linear interpolation for less

than two missing hours or a mean NEE value over one nighttime period. Nighttime EC-NEE was assigned as nighttime ecosystem respiration (R_{eco}), and daytime R_{eco} was derived from averaging R_{eco} over two adjacent nighttime periods, similar to Restrepo-Coupe et al. (2013). Then, gross primary productivity (GPP) was obtained by subtracting EC-NEE from R_{eco}. We adopted the above NEE partitioning method because nighttime R_{eco} did not correlate well with nighttime air temperature, which is needed for commonly used methods (e.g., the nighttime method (Reichstein et al., 2005), the daytime method (Lasslop et al., 2010) and modified daytime methods (Keenan et al., 2019)). In this study, we interpret EC-GPP (hereafter GPP) as gross ecosystem productivity (GEP).

3.5 | STILT simulations

3.5.1 | STILT model description

The Stochastic Time Inverted Lagrangian Transport (STILT) model (Lin et al., 2003) is useful for diagnosing the impact of surface emissions at a specific measurement location or receptor by resolving transport in the near-field (i.e., the surface with which the planetary boundary layer air has had contact with). STILT simulates the transport in the near-field by following the time evolution of an ensemble of particles (to be interpreted as an air parcel) and by interpolating meteorological fields to the sub-grid location of each particle. Turbulent motions in the planetary boundary layer (PBL) are modelled as a Markov chain process using turbulent velocity statistics (Lin et al., 2003). Moist convection in STILT uses vertical profiles of convective mass fluxes within updrafts and downdrafts, as well as entrainment and detrainment fluxes into and out of the up- and downdrafts (for details, see Nehrkorn et al., 2010). Vertical profiles of in-cloud mass fluxes are derived from the driving meteorological fields using the Tiedtke scheme (Tiedtke, 1989).

The time-inverted feature of the model refers to the capability of resolving the near-field transport of the particle ensemble prior to its arrival at the receptor location. In this study, the model was run at hourly resolution for the six-year period from 2014 to 2019. Every hour a 100-particle ensemble was released at the receptor height of 80 m above ground, and the back trajectories were calculated for the preceding 10 days to ensure most backward trajectories have left the continent, such that the footprints represent the full influence of surface fluxes on measurements at ATTO. The difference between the modelled receptor height and the air inlet is only 1 meter, which we assume can be neglected. The model was driven by 3-hourly meteorological fields from ECMWF short-term forecasts (following the contemporary IFS cycle development; for more info see `https://www.ecmwf.int/en/publications/ifs-documentation`). The original meteorological fields were preprocessed and interpolated to a spatial resolution of 0.25° by 0.25°, covering South America between 20°S–15°N latitude and 85°W–35°W longitude bands. The original vertical structure was maintained, however only the 89 lowest of the 137 total levels were used, limiting the top model level to an altitude of about 21 km.

3.5.2 | Seasonally-averaged footprint calculation

To better interpret our measurements and attribute signals to particular regions, spatially explicit surface influence maps or footprints were calculated using the STILT model. From the back trajectory particle ensembles we derived hourly-gridded footprints. The footprints are derived at higher spatial resolution (1/12° by 1/8°) than the driving meteorological data, and they can be defined as the flux sensitivity of mole fractions measured at the receptor location, with units of ppm per μmol m^{-2} s^{-1}. To obtain the seasonally-averaged footprints, we first filtered for daytime (i.e., 13:00-17:00 LT at the receptor) values to ensure well-mixed convective conditions at the measurement location. These individual hourly footprints were aggregated to a climatological monthly mean. From these monthly means we

averaged over: November, December, January (NDJ), February, March, April (FMA), May, June, July (MJJ) and August, September and October (ASO). The averaging periods were chosen in this way to allow a good distinction between wet and dry seasons (FMA and ASO), as well as the transition periods in between (NDJ and MJJ). The monthly climatology of concentration footprints generated for this study is available at `http://doi.org/10.17871/atto.208.8.811`.

The regional extent of the seasonally-averaged footprints is shown in Figure 6 to provide an idea of the dominant vegetation types within the areas of influence. The 50th percentile footprint during NDJ and FMA covers an area of mainly intact forest, whereas in MJJ and ASO the footprints cover areas characterized by a larger presence of disturbed forest, located on the southern bank of the Amazon River. The area of the 50th percentile footprint increases from 208,058 km^2 in NDJ to 236,969 km^2 in FMA and decreases from 244,482 km^2 in MJJ to 207,812 km^2 in ASO. Note that the Cerrado and Caatinga biomes (semiarid ecosystems), are within the 75th percentile footprint in MJJ and ASO, although their relative influence on the signals measured at ATTO is estimated to be low.

3.5.3 | STILT tracer simulations

Lateral Boundary Conditions (LBC)

As we are dealing with an atmospheric transport model within a limited domain, we have to consider the influence of the air masses entering it at its borders (LBC, Lateral Boundary Conditions) to compare the simulated mole fractions to in situ observations. This additional signal, hereafter also referred to as "background", is added in STILT to the CO_2 mole fractions related to fluxes from within the domain. In the case of ATTO, it is almost exclusively advected from the northeastern or eastern border of our domain (see Figure 6). The LBC include the global information that influences our domain of interest, such as the increasing trend due to fossil fuel burning and variations on seasonal and synoptic scales. In this study, we have used the Jena Carboscope (s04ocv4.3) as our LBC. We refer the reader to Rödenbeck et al. (2003) and to `http://www.bgc-jena.mpg.de/CarboScope/` to get more details on the data assimilated in this system.

The validity of the LBC is a fundamental aspect in our tracer simulations. To assess this validity and potential biases, we evaluated the 3D fields of CO_2 used as LBC at three background stations located at the east and northeast of our regional domain: Ragged Point Barbados (RPB, 13.16°N, 59.43°W), Ascension Island (ASC, 7.94°S, 14.35°W) and Cape Verde (CVR, 15.12°N, 23.60°W). We sampled the original global fields at the location of each station and calculated the difference between the simulated and observed mole fractions (see Figure S3). Since the data from the above stations were assimilated in the Jena CarboScope inversion system, they have small Mean Bias Errors (MBE) (-0.09 ± 0.26 ppm at RPB, -0.036 ± 0.28 ppm at ASC and -0.176 ± 0.8 ppm at CVR). Even though these small MBE indicate a strong constraint on the LBC, we have bias corrected the LBC used to calculate the observed regional signal. The magnitude of the bias-correction will be shown in the Results section. We define an observed regional signal ($\Delta CO_{2_{obs}}$, which is bias-corrected) and a simulated regional signal ($\Delta CO_{2_{sim}}$). The first is calculated by subtracting the LBC from the measured CO_2 mole fractions, and the second by leaving the LBC tracer out of equations 1 and 2.

Input fluxes

To obtain simulated mole fractions at the tower location, we coupled the footprints with the surface fluxes at hourly resolution. By adding all the tracer components and the LBC, we can obtain multiple realizations of simulated CO_2 mole fractions at the ATTO site that can be compared to observations, and assess how the underlying fluxes affect the simulated signal. To account for all the sources and sinks of CO_2 and their uncertainties in Amazonia, we use a wide range of available data sets, including both optimized (i.e., resulting from atmospheric inverse modeling) and non-optimized NEE flux fields (see Table 2).

Equations 1 and 2 show the main tracer components that were added to obtain the integrated CO_2 mole fractions at ATTO. The subscripts represent the flux categories associated with different processes and the * indicates we use multiple NEE sources for each equation as we explain below. The complete overview of input flux fields used for each tracer is given in Table 2.

$$CO_{2_{TopDown}}[ppm] = \sum CO_{2_k}, \quad k = LBC, NEE^{*}_{TopDown}, ocean, fires, fossilfuel \tag{1}$$

$$CO_{2_{BotUp}}[ppm] = \sum CO_{2_k}, \quad k = LBC, NEE^{*}_{BotUp}, ocean, fires, rivers, fossilfuel \tag{2}$$

As vegetation dominates the CO_2 exchange within our domain, we used five Net Ecosystem Exchange (NEE) data sets, three of which are optimized using an atmospheric inversion system. The atmospheric inversion system (Peters et al., 2005) utilizes available in situ and remote sensing measurements for the assimilation process; it should be noted, however, that observations from ATTO were not assimilated in any of the products discussed here. In equations 1 and 2, NEE is replaced according to the list in Table 2 and thus we obtain five STILT-model results for simulated CO_2 mole fractions at ATTO.

The optimized NEE flux fields (i.e. Top-down) were produced using different settings but the same CarbonTracker Data Assimilation System (CTDAS, van der Laan-Luijkx et al. (2017)). All inversions use the transport model TM5 (Krol et al., 2005), where the default run (CTE2020) uses a global transport resolution of 3°x 2°with 1°x 1°zoom regions over Europe and North America, and two South-America-specific setups of the system (CT-SAM, van der Laan-Luijkx et al. (2015); Koren (2020): CT-SAM-OCO2 and CT-SAM-Flask) use a global resolution of 6°x 4°with a nested zoom over South America of 3°x 2°and 1°x 1°. The three inversions also use different sets of atmospheric CO_2 data for the assimilation: surface flask measurements from ObsPack GLOBALVIEWplus 5.0 (available here: `https://doi.org/10.25925/20190812`) (CTE2020), the same GLOBALVIEWplus 5.0 but with additional aircraft profiles (Gatti et al., 2014) from different locations in Amazonia (CT-SAM-Flask), or OCO2 satellite column retrievals (CT-SAM-OCO2). For the CT-SAM-OCO2 the NASA retrieval v9r was used (`https://docserver.gesdisc.eosdis.nasa.gov/public/project/OCO/OCO2_DUG.V9.pdf`). The column observations were aggregated to 10-second super observations (following the method described in (Crowell et al., 2019)) and retrievals above water were excluded. CT-SAM optimizes NEE on a gridded state vector of 1°x 1°over South America, whereas CTE2020 optimizes NEE in the region using larger "ecoregions" following the plant-functional types in the prior biosphere model (SiBCASA, (Schaefer et al., 2008)). Note that the driving meteorology in CTE2020 uses ERA5 (C3S, 2017) instead of ERA-interim, as in CT-SAM-Flask and CT-SAM-OCO2.

The non-optimized NEE fluxes (VPRM and FLUXCOM, i.e. bottom-up) use different approaches. The Vegetation Photosynthesis and Respiration model (VPRM) estimates NEE using a simple diagnostic light-use-efficiency model driven by the Enhanced Vegetation Index (EVI) and Land Surface Water Index (LSWI), derived from surface reflectance measured by the Moderate Resolution Imaging Spectroradiometer (MODIS), together with 2-m air temperature and shortwave radiation at the surface provided from the meteorological model (Mahadevan et al., 2008), in this case STILT. Two parameters per vegetation type (Jung et al., 2006) are optimized based on eddy covariance measurements from 9 sites between 2001 and 2010, obtained from the LBA-ECO repository (`https://daac.ornl.gov/daacdata/lba/carbon_dynamics/CD32_Brazil_Flux_Network/data/`, last access: 19 October 2020). The FLUXCOM product is derived from up-scaling site-level data (FLUXNET, `http://fluxnet.fluxdata.org/` (last access: 29 September 2020)) to global scales by using a set of predictors which are fed to a random forest regression (Bodesheim et al., 2018). The reader is referred to Bodesheim et al. (2018) and Jung et al. (2020) for more information on the predictors

TABLE 2 Input fluxes and lateral boundary condition data sets used in STILT. Column "Input type" indicates whether the fluxes are based on atmospheric inversions (prefix "Opt").

Tracer	Product Name	Input type	Time coverage	Notes	Reference
LBC	Jena CarboScope (s04ocv4.3)	mole fractions	2014-2019	LBC - lateral boundary condition	Rödenbeck et al. (2003)
Ocean	CTE2020	Opt flux	2014-2019	Top-down (TD) and Opt. atm. inversion	van der Laan-Luijkx et al. (2017)
NEE	CTE2020	Opt flux	2014-2019	TD and Opt.	van der Laan-Luijkx et al. (2017)
NEE	FLUXCOM	Flux	2014-2019	Bottom-up (BU)	Bodesheim et al. (2018)
NEE	VPRM	Flux, online	2014-2019	BU	Mahadevan et al. (2008)
NEE	CT-SAM-OCO2	Opt flux	2015-2017	TD, not used for other years (Opt)	Koren (2020)
NEE	CT-SAM-Flask	Opt flux	2014-2017	TD, 2018 and 2019, 2008-2017 average (Opt)	Koren (2020)
Rivers	ORCHILEAK	Flux	2014-2019	1980-2010 - Climatology	Hastie et al. (2019)
Biomass burning	GFAS	Emissions	2014-2019		Kaiser et al. (2012)
Fossil Fuels	EDGAR 4.3.2	Emissions	Annual mean	All sectors, aggregated	Janssens-Maenhout et al. (2017)

and the up-scaling methods.

We use river CO_2 fluxes from the updated version (Hastie et al., 2019) of the ORCHILEAK model (Lauerwald et al., 2017), which uses a high spatial resolution (100 m) wetland distribution map (Hess et al., 2015). We only add the river flux component to the bottom-up simulations, as for the top-down simulations the river signal should be captured by the assimilated observations (Kondo et al., 2020). In order to avoid double counting of fluxes from floodplains, which could be captured by VPRM and FLUXCOM during a low water stage, we only used the river CO_2 evasion component from the ORCHILEAK model. The tracers that are not varied in equations 1 and 2 (i.e., ocean, fires, fossil fuel) are always added to the simulated mole fraction of each STILT-model realization.

We also simulated the anthropogenic signal component using the annual mean emissions from EDGAR v4.3.2 (Janssens-Maenhout et al., 2017) reported for 2012; original gridded emissions (0.1°x 0.1°spatial resolution) from all fossil fuel sectors were aggregated into an emission field of a single tracer. Since anthropogenic emissions are of minor importance in our domain we assumed constant annual emissions in our simulations. For the contribution of biomass burning or fires we use daily emissions from the Global Fire Assimilation System (GFAS) at 0.1°x 0.1°spatial resolution (Kaiser et al., 2012). Last but not least, we use optimized oceanic CO_2 fluxes from CTE2020. It is worth mentioning that in CTE2020, different from previous releases, the ocean prior flux is taken from the Jena Carboscope system.

3.5.4 | Input flux adjustments for STILT simulations

The input fluxes have been converted for use in STILT into units of μmol m^{-2} s^{-1}. Furthermore, we have adjusted the weekly mean posterior NEE fluxes of CTE2020, CT-SAM-OCO2 and CT-SAM-Flask to represent the original diurnal variability of its prior biosphere model (SiBCASA) before using them as input in STILT. Equation 3 describes this adjustment, which projects the original 3-hourly deviations from the monthly average diurnal cycle back onto the weekly mean posterior flux. For CTE2020, equation 3 was used for each week (k) that fluxes are available, in which the deviation of the 3-hourly (j=1,..8) flux from the corresponding monthly (i) mean is added to the weekly posterior. For the CT-SAM-OCO2 and CT-SAM-Flask the prior and diurnal mean NEE in equation 3 (1^{st} and 2^{nd} term on the right-hand side) were replaced by its climatology for each month (i=1-12), as their multi-annual record was smaller and included an ENSO extreme event. This adjustment was performed in order to convert monthly optimized NEE fluxes (CTE2020, CT-SAM-OCO2 and CT-SAM-Flask) to hourly resolution and thus couple them with the hourly footprints. This is important because the diurnal variability in atmospheric transport has to be considered for more accurate simulations. We consider that the adjustment is precise enough because the simulated diurnal cycle of CO2

at the tower resembles that of the other simulations which are originally provided as hourly fluxes. This is shown in Figure S4.

$$NEE_{post_{3h_{k,j}}} = (NEE_{prior_{3h_{k,j}}} - DiurnalMeanNEE_{prior_{3h_{i,j}}}) + NEE_{post_{Weekly_k}} \quad (3)$$

4 | RESULTS

4.1 | ATTO atmospheric CO_2 time series

The observed CO_2 trend (Figure 6a) at ATTO for the 6-year record is 2.38 ppm year^{-1} (2.18-2.60 95% CI), which is very similar to the mean global CO_2 growth rate of 2.49 ± 0.08 ppm year^{-1} reported by Dlugokencky and Tans (2020) for the same time period. From the monthly record, we can highlight the wet seasons of 2016 and 2019 as two distinctive events of important inter-annual variability in which the footprint of the tower was likely a source of CO_2 to the atmosphere. In the transition from wet to dry seasons, our measurements reach a peak that is followed by a consistent decline throughout the dry season. On average, this decline has an onset in July and August. We also note that the monthly variability is lower in the dry season than in the wet season, strengthening the consistency of the dry season decline.

The simulated background mole fractions (LBC-CScope) have a marked seasonality, reaching the highest values during the wet season, indicating that the air masses coming into our domain are enriched with CO_2. This is in accordance with Figure 6, in which we showed that the surface influence during the wet season is oriented to the northeast, bringing air from the northern hemisphere. When subtracting the simulated background mole fractions from our measurements, we can diagnose specifically the regional signal of CO_2, defined as $\Delta CO2_{obs}$ in Section 3.5.3. The seasonal cycle of $\Delta CO2_{obs}$ (Figure 6b) has an amplitude of 4.14 ppm (default) and 4.11 ppm (bias-corrected) and two distinct periods in which the signal at ATTO is below the LBC tracer (< 0 ppm). It is worth mentioning that $\Delta CO2_{obs}$ contains information about the real fluxes in our domain, but it also has an atmospheric transport component, making it difficult to interpret it solely as a source (> 0 ppm) or an uptake (< 0 ppm) of CO_2.

As $\Delta CO2_{obs}$ is the object of study in this paper, we have assessed its uncertainty by obtaining a range between an independent LBC estimate and a bias corrected version of the LBC-CScope. The first, was calculated by taking the measurements at the background stations ASC and RPB and interpolating a new LBC based on the latitude of the STILT-particles once they exit our domain. To account for the minor biases of the LBC-CScope at the background stations, we have bias corrected the LBC-CScope, the magnitude of this correction is shown in Figure 6a by the dashed blue line. The min-max range of these two $\Delta CO2_{obs}$ estimates is lower than the inter-annual monthly standard deviation of the $\Delta CO2_{obs}$, which strengthens the robustness of this quantity. For the rest of this study we will use the bias-corrected $\Delta CO2_{obs}$.

4.1.1 | Drivers of seasonal variability

$\Delta CO2_{obs}$ is affected by local (eddy covariance scale) and non-local scales (concentration footprint scale). At the local scale, we confront the $\Delta CO2_{obs-bio}$ with the EC-NEE in Figure 6a. The $\Delta CO2_{obs-bio}$ was calculated using the bias-corrected $\Delta CO2_{obs}$ and subtracting the simulated contribution of rivers, fires, fossil fuel and ocean. The phase of the seasonality of $\Delta CO2_{obs-bio}$ differs from that of EC-NEE, mainly in January, February and March and in October, November and December. From April to July EC-NEE exhibits an increasing source that can influence the increasing

pattern in $\Delta CO_{2_{obs-bio}}$. The dry season decline in $\Delta CO_{2_{obs-bio}}$ can be partly attributed to a decrease in EC-NEE which is triggered mainly by a reduction in R_{eco} from May to August and a gradual increase in GPP after August (Figure 6b). The effect of atmospheric transport is also important here. For example, the height of the PBL is a variable that affects the measured CO_2 mole fractions at the tower. The PBL height tends to be deeper during the dry season (1300-1500 m) than in the wet season (1100-1200 m), which means that the volume in which CO_2 mole fractions are diluted is larger, causing more negative $\Delta CO_{2_{obs-bio}}$. This example illustrates how the seasonal effects of the footprint and the PBL height can influence $\Delta CO_{2_{obs-bio}}$. The observed phase differences indicate that $\Delta CO_{2_{obs-bio}}$ can decouple from the local EC-NEE in some months of the year, suggesting that the seasonality in $\Delta CO_{2_{obs-bio}}$ is controlled by overlapping effects of local and non-local drivers.

One of the most important non-local drivers of $\Delta CO_{2_{obs-bio}}$ is the heterogeneity of NEE across the seasonally-changing footprint area. The amplitude of the seasonal cycle of EC-NEE in Amazonia varies along the precipitation gradient (Saleska et al., 2009). Locations with a higher mean annual precipitation (MAP) (>2500 mm yr^{-1}), like K34 (2.61°S, 60.21°W) have a smaller seasonal cycle amplitude, whereas drier sites (2000-2200 mm yr^{-1}) further east in the Tapajós National Forest (K67 and K83) display a more pronounced seasonal cycle (Saleska et al., 2009). EC-NEE at ATTO (2.14°S, 58.99°W) shows interesting patterns as it falls between the range mentioned above, with a MAP of 2382 mm yr^{-1} and a seasonal EC-NEE range of approximately 60 g C m^{-2} $month^{-1}$ (600 kg C ha^{-1} $month^{-1}$). Thus, we observed a seasonal variability with a midyear source peak, different from the sustained net uptake throughout the year reported for K34 by Restrepo-Coupe et al. (2017). ATTO is located about 140 km northeast of K34: the sites are relatively close, yet exhibit different MAP and seasonal EC-NEE patterns. ATTO EC-NEE is more similar to that measured at the Tapajós National forest in having a dry season decline, reaching neutrality in September and October (Saleska et al., 2003; Goulden et al., 2004; Baker et al., 2008; Hayek et al., 2018), but it differs in that the wet season shows on average a weak source, which after March increases towards a seasonal peak in May. Interestingly, the ATTO EC-NEE seasonality has a similar phase to the Caxiuanã (CAX) site (Restrepo-Coupe et al., 2017). Following the classification in Saleska et al. (2009), the EC-NEE amplitude at ATTO falls close to the sites where R_{eco} is the most important factor.

From the $\Delta CO_{2_{obs-bio}}$ perspective, R_{eco} can be important from March to July, when EC-NEE and $\Delta CO_{2_{obs-bio}}$ are in phase. Further inspection of the local processes at ATTO indicates that R_{eco} correlates significantly with EC-NEE (r=0.55, p-value < 0.01). Furthermore, river CO_2 evasion (Figure 6d) could also contribute to $\Delta CO_{2_{obs}}$, mainly from April to July, with a peak contribution of 1.7 ppm in May and June. Simulated aquatic CO_2 signals are in phase with water levels as shown by the Equivalent Water Height anomalies. We consider this timing realistic, as CO_2 evasion from rivers and floodplains is enhanced at high water stages (Richey et al., 2002; Amaral et al., 2020), due to larger inundation areas and an increased water depth that leads to more respiration in the water column (Devol et al., 1995; Forsberg et al., 2017). Considering that the tower's STILT footprint during MJJ covers the main branch of the Amazon River (see Figure 6), we believe aquatic signals play an important role when interpreting the seasonal cycle of CO_2 measurements at ATTO.

GPP was found to be negatively correlated with EC-NEE but not significantly (r=-0.14, p-value=0.21). Therefore, the offset of photosynthesis by R_{eco} suggests that the first is less important for $\Delta CO_{2_{obs-bio}}$ at the local scale. Nevertheless, the local processes controlling GPP during the dry and wet seasons are worth highlighting here. The gradual rise in GPP during the dry season is driven by increasing light availability and a younger age distribution of leaves in the canopy (Figure 6c). Note that PAR increases simultaneously with a decline in the old class of leaf area index (LAI) and the increment of the mature and young LAI classes. Such leaf demography dynamics are similar to what Wu et al. (2016) showed for other sites in Amazonia, and consistent with the dry season green-up reported by several in-situ (Restrepo-Coupe et al., 2013; Lopes et al., 2016) and regional (Huete et al., 2006; Doughty et al.,

2019) studies. Moreover, Wu et al. (2016) demonstrated that mature leaves are the most light-use efficient with the highest photosynthetic capacity (mol CO_2 mol^{-1} $photon^{-1}$) of all leaf age classes. Thus, the seasonal shift in LAI age classes produces a younger age composition of the canopy relative to the wet season, which on average has a higher photosynthetic capacity per leaf area (Wu et al., 2016; Albert et al., 2018). In addition, reduced GEP (interpreted here as GPP) for June and July was reported by Restrepo-Coupe et al. (2013) and Wu et al. (2016) for equatorial sites (e.g. Tapajós National Forest (K67), Cuieras Reserve (K34), and Caxiuana National Forest (CAX).

4.1.2 | Drivers of inter-annual variability

Although our CO_2 time series is rather short for inferring inter-annual patterns, we present the response of $\Delta CO_{2_{obs}}$ and $\Delta CO_{2_{obs-bio}}$ to the 2015/2016 El Niño-induced drought (Figure 6a). Interestingly, the standardized anomalies of $\Delta CO_{2_{obs}}$ and $\Delta CO_{2_{obs-bio}}$ follow the same pattern, suggesting that the inter-annual variability is controlled by the vegetation signal and that contributions of rivers, fires, fossil fuels and ocean are negligible at this scale. For this reason, in the rest of this Section we refer to $\Delta CO_{2_{obs}}$ only, but the findings apply equally to $\Delta CO_{2_{obs-bio}}$.

The >+1σ anomaly of $\Delta CO_{2_{obs}}$ in MJJ coincides with the onset of the El Niño, which started in June of 2015, with values above 1 according to the Multivariate El Niño Index (MEI) (Figure 6b). In the dry season of the same year (ASO), we observe a -1σ anomaly, illustrating a variable response of $\Delta CO_{2_{obs}}$ to El Niño in 2015. In contrast, in 2016 our observations reveal two >+1.5σ anomalies, centered in the wet and dry seasons. Note that El Niño lasted until May in 2016, but the effects in $\Delta CO_{2_{obs}}$ seemed to persist well into the dry season of 2016.

It is interesting to note that the local EC-NEE (Figure 6a) anomaly is not always in phase with that of $\Delta CO_{2_{obs}}$. In 2015 the EC-NEE anomaly was in opposite sign to that of $\Delta CO_{2_{obs}}$ during MJJ and ASO, while in 2016 they followed similar patterns. Such differences in phase between EC-NEE and $\Delta CO_{2_{obs}}$ anomalies suggest that in 2015 the effects of El Niño at the EC-NEE scale were apparent only after ASO, whereas in the $\Delta CO_{2_{obs}}$ record it was already evident in MJJ. Therefore, the 2015 anomalies appear to be driven by a non-local (i.e. larger than the EC-NEE footprint) response to the El Niño. In contrast, the contribution to the positive anomalies in 2016 appears to be both at the local and non-local scales.

The variable response of the $\Delta CO_{2_{obs}}$ anomalies in 2015 are marked by an erratic behavior, showing opposing signs in MJJ (+) and ASO (-). The MJJ event is driven by an above average value in July, whereas that in ASO is pulled down by a negative value in September and October (not shown). Our eddy covariance data suggest that the $\Delta CO_{2_{obs}}$ positive anomaly in July can not be attributed to a local source of carbon, as the EC-NEE (see Figure S5) for 2015 was within the seasonal variability of the 2014-2019 record. The negative anomaly in ASO, can not be explain by local factors either. A reduction in the observed CO_2 mole fractions due to a deeper boundary layer height, a 15% percent increase with respect to 2014 as shown by Carneiro and Fisch (2020), is likely but non-local factors are yet to be studied. Interestingly, the GPP reductions in 2015 reported in Koren et al. (2018) and van Schaik et al. (2018) for the region that overlaps with our MJJ footprint (i.e. Region B in that study) have an onset in October, failing to explain our July observation and indicating that the effect of the extreme heat and drought had a late onset at ATTO.

The positive anomaly in $\Delta CO_{2_{obs}}$ during the dry season of 2016 has local and non-local contributions. Locally, a source of carbon in our EC-NEE record, driven by a higher than normal R_{eco} (Figure S5), can explain the $\Delta CO_{2_{obs}}$ 2016-ASO anomaly. Non-local drivers of this anomaly are attributed to a drought legacy effect (Kannenberg et al., 2020) that has been already characterized by Koren (2020) using atmospheric inverse modeling and remote sensing. Koren (2020) reported basin-wide positive anomalies in top-down-NEE and reductions in remote sensing proxies for GPP in the dry season of 2016. Persistent soil moisture depletion following the 2015/16 El Niño was put forward as a potential mechanism driving this legacy drought. A contributing factor to this 2016-dry-season anomaly, based on

the results by Wu et al. (2016) and Gonçalves et al. (2020), is that drought in 2015 caused some trees (approximately 15%) to undergo an anomalous leaf flush in March of 2016 (see Figure S6). This precocious flush altered the normal leaf age distribution over the following months, such that the abundance of photosynthetically efficient mature-stage leaves (2-6 months of age) was spread out over a longer period.

The meteorological effects of El Niño at local scale were measured later in 2015. Positive anomalies in air temperature within and above the canopy together with soil temperature (Figure 6c) reached values close to +2σ from November of 2015 to February of 2016. The negative soil moisture anomalies in the last four months of 2015 were driven by the negative precipitation anomalies during the same time (Figure 6d,e). The soil moisture anomalies at 40 cm and 100 cm bounced back to values higher than -1σ in March 2016. However, even when precipitation returned to close-to-climatology values in February and March 2016, soil moisture at 10 cm depth did not fully recover until late 2016. This pattern shows a fast recovery in deep soil moisture compared to a persistent (<-1σ) soil moisture anomaly at 10 cm depth. The re-wetting of deeper layers, together with a still high soil temperature anomaly at 20 and 40 cm depth, could have reactivated heterotrophic respiration leading to above-average soil respiration rates during the wet season of 2016 (see Figure S5).

The $\Delta CO_{2_{obs}}$ anomalies in the transition months of NDJ in 2018 and 2019 occurred in the absence of a large scale climate-driven phenomenon. Based on the EC-NEE response, it seems that both $\Delta CO_{2_{obs}}$ anomalies are due to non-local signals. During the 2018-NDJ event, all meteorological variables (air temperature, soil moisture and temperature, and precipitation) were within the 1σ range. To interpret the signals in 2019, it is worth mentioning two aspects. First, the 2019-NDJ average contains values only for November and December, as January data were not yet available at the time of writing. Second, the year 2019 was characterized by widespread fires driven by deforestation which began early in the year (Barlow et al., 2020). Thus, we suggest that the 2019-NDJ positive anomaly could have a contribution from fires, but the magnitude could be reduced when the January average is included.

4.2 | STILT tagged tracer simulations

4.2.1 | Simulated CO_2 and spatial distribution at seasonal scale

At the ATTO site, a clear seasonal variation of the footprint throughout the year (Figure 6a) can be observed, consistent with the large scale atmospheric circulation of the intertropical convergence zone (ITCZ) previously described in Andreae et al. (2012) and Pöhlker et al. (2019). The seasonal atmospheric circulation affects the mole fractions measured at ATTO by varying the areas of near- and far-field influence of the surface fluxes and also the origin of the background air masses. In general, during the wet season ATTO is located to the north of the ITCZ and is under the influence of the air coming from the Northern Hemisphere (NH), whereas during the dry season, the station is located south of the ITCZ, and thus the long range transport is from the Southern Hemisphere (SH) (Andreae et al., 2015). It is worth highlighting that during MJJ and ASO the main branch of the Amazon River is well covered by the 50th and 75th footprint percentiles.

The different NEE fluxes used as inputs in STILT show large spatial variability amongst them (Figure 6b-d). While CTE2020 and CT-SAM-Flask follow a similar spatial pattern, CT-SAM-OCO2 tends to predict a larger source of carbon to the atmosphere in MJJ. When comparing the bottom-up fluxes (Figure 6e-f) to those resulting from atmospheric inversions, it is clear that the former shows a stronger sink, which is particularly visible in the FLUXCOM data. The main differences between FLUXCOM and VPRM are the source regions in NDJ and ASO, more pronounced in FLUXCOM than in VPRM. Despite the aforementioned differences, in the core of the dry season (ASO) all products are consistent (with varying extent and magnitude) in the source regions in northeastern Brazil, in the states of Ceará, Pernambuco,

Bahía, Piauí and Tocantins (see Figure S7 for the names and locations of the northeastern states of Brazil).

We find that none of the simulations accurately capture the amplitude of $\Delta CO_{2_{obs}}$. Only in the case of FLUXCOM, does the shape of the seasonal cycle show a decline in the dry season and a wet-to-dry season increase similar to the pattern observerd at ATTO. The latter increase is also better predicted if the original product is augmented with additional fluvial fluxes (compare both panels in Figure 6). However, FLUXCOM-driven mole fractions predicted by our model are constantly lower than our measurements by 5 ppm, indicating a strong and persistent uptake of CO_2 (negative NEE) as shown in Figure 6. Such a strong sink was expected, as this product was previously found to have a too strong tropical carbon sink, due to a mixture of systematic biases in the eddy-covariance data used in upscaling, and the lack of site history effects on NEE (Jung et al., 2020). Simulations of $\Delta CO_{2_{sim}}$ based on VPRM, CTE2020, CT-SAM-Flask and CT-SAM-OCO2 fluxes show a very different seasonal cycle than $\Delta CO_{2_{obs}}$, showing an earlier and more rapid drop to a minimum in July. In terms of the amplitude of the seasonal cycle, VPRM predicts the largest with 5.94 ppm, followed by CTE2020 with 5.88 ppm, CT-SAM-OCO2 with 5.07 ppm, CT-SAM-Flask with 4.94 ppm and finally FLUXCOM with 3.21 ppm. The last two are the closest to the observed $\Delta CO_{2_{obs}}$ of 4.14 ppm.

The accuracy of the VPRM simulations was worse than expected considering that the model parameters were calibrated using eddy covariance measurements at several sites within Amazonia (Mahadevan et al., 2008). We find that the dry season increase in VPRM-$\Delta CO_{2_{sim}}$ could be triggered by increasing simulated R_{eco} associated with increasing temperature. VPRM represents R_{eco} as a linear function of temperature and does not include the effects of moisture (Mahadevan et al., 2008). Furthermore, the decrease in VPRM-$\Delta CO_{2_{sim}}$ from May to July, which anticipates that of $\Delta CO_{2_{obs}}$ by a month, could also be associated with the lack of moisture effects in R_{eco}. Note that the eddy covariance R_{eco} is higher than GPP from May to June in Figure 6b, suggesting an overall source of carbon to the atmosphere.

4.2.2 | Simulated inter-annual variability and tracer contribution

In general, the observed inter-annual variability is not well captured by our STILT simulations (Figure 6a). In particular for the 2015 and 2016 anomalies associated with El Niño, the simulations show either an anticipation of the anomaly (i.e. 2015-NDJ) or output a signal with an opposite sign (i.e. 2016-ASO). Despite the spread between models in 2014-MJJ, 2015-MJJ and 2018-FMA, it is worth highlighting the general agreement between them, not only in 2015-NDJ and 2016-ASO but also in 2017-ASO, 2018-ASO, 2019-ASO and 2019-NDJ. The latter indicates that the disagreement between simulations is largest in the first part of the year, in which the influence of river CO_2 is predicted to be highest.

The influence of rivers, fires, fossil fuel emissions and ocean fluxes on the simulated CO_2 signal is very small compared to that of NEE (Figure 6b-e). Note that the simulated NEE contribution in general tends to show a sink of CO_2, mainly in the transition from wet to dry season, in contrast to $\Delta CO_{2_{obs}}$ and $\Delta CO_{2_{bio}}$. For the $\Delta CO_{2_{bio}}$ the signal from rivers, fires, fossil fuels and ocean was subtracted, which did not change the seasonal pattern when compared to $\Delta CO_{2_{obs}}$. Rivers contribute with 1 to 2 ppm depending on the month of the year. Note that the spatial resolution of the gridded flux for rivers is coarse ($1^\circ \times 1^\circ$) and we have used a monthly climatology from Hastie et al. (2019) in STILT, thus the variable magnitude from year to year in the river tracer is mainly due to atmospheric transport. Fires and anthropogenic emissions (fossil fuels in equations 1, 2) add up to a contribution ranging from 0.2 to 0.4 ppm, concentrated in the dry season. The ocean is the least significant tracer component, contributing less than 0.1 ppm to the regional signal, reaching the highest values during NDJ. These simulations highlight the relevance of CO_2 evasion at the ATTO site.

When evaluating the model performance at a monthly scale, the CT-SAM-OCO2 simulation was the best, with an RMSE of 4.15 ppm. Note that the CT-SAM-OCO2 simulations were performed only for three years (i.e. 2015-2017).

The VPRM and the CT-SAM-Flask followed with RMSE values of 4.21 ppm and 4.63 ppm respectively. CTE2020 and FLUXCOM had higher RMSE values with 4.96 ppm and 5.6 ppm. These RMSE scores are indicative of regional fluxes not covered by our footprints or the LBC, or from differences in vertical transport between the STILT model used for the footprints relative to the TM5 model (used in CarbonTracker).

5 | DISCUSSION

5.1 | Decomposing the $\Delta CO_{2_{obs}}$ signal

We showed that $\Delta CO_{2_{obs}}$ is controlled by local and non-local factors. The phase match/mismatch at seasonal and inter-annual scales between EC-NEE and $\Delta CO_{2_{obs}}$ was described as an indicator of the different spatial extents driving $\Delta CO_{2_{obs}}$. Amongst the local factors analyzed was EC-NEE, which was partitioned into GPP and R_{eco} to better understand the underlying processes contributing to the local net flux. GPP and R_{eco} presented a considerable seasonal variation, mainly characterized by a R_{eco}-dominated wet season and a late dry season increase in both GPP and R_{eco}. Seasonally, we found that EC-NEE was mainly controlled by R_{eco}. However, it is worth mentioning that when leaving 2015 and 2016 out of our analysis, we see a clear sink in the EC-NEE during the dry season. In contrast, focusing only on 2015 and 2016 we observe a suppression of GPP during the dry season and EC-NEE shows a sustained source as R_{eco} is always larger than GPP. Therefore, seasonally we observed a larger role of R_{eco} and a clear effect of the 2015/2016 El Niño in GPP, R_{eco}, EC-NEE and $\Delta CO_{2_{obs}}$ (see Figure 6).

At a more regional scale, the effects of the 2015/2016 El Niño-induced drought in Amazonia have been studied from multiple perspectives. The immediate effects of the drought (namely occurring in 2015 and 2016) caused reductions in GPP (Liu et al., 2017; van Schaik et al., 2018) (in line with our local measurements) and sun-induced fluorescence (SiF) (Koren et al., 2018; Castro et al., 2020). The study of Castro et al. (2020), which described the effect of the 2015/2016-El Niño event on SiF across the Amazon basin, sheds light on the variable response of vegetation to drought. At the regional scale, they found a widespread reduction in SiF, yet at the eco-region scale where ATTO is located, SiF reductions were comparatively less. However, Doughty et al. (2021) found positive anomalies in SiF and GPP at the Amazon basin scale and at the grid cell in which ATTO is located. Therefore, the debate about the sign of the anomaly in 2015 remains open. The effects of the 2015/2016 El Niño drought caused long-term impacts on vegetation, Wigneron et al. (2020) found that the above-ground carbon stocks did not recover until 2017. Furthermore, top-down studies of previous droughts (Gatti et al., 2014; van der Laan-Luijkx et al., 2015) have shown that the Amazon carbon budget can turn from almost neutral in a wet year (i.e., 2011), into a source during drought (i.e., 2010). A reduction in biospheric uptake and an increase in CO_2 fire emissions were suggested as the main causes for the regional response in 2010, which was well captured by widespread aircraft measurements of CO_2 concentrations over the basin. Given these previous findings, local/non-local GPP reductions, long-term vegetation effects and fire emissions are factors that can in principle influence $\Delta CO_{2_{obs}}$, in addition to the role of R_{eco} and river signals, which were presented in our results. However, for the present study we found that even during the 2015/2016-El Niño the fire contribution to the local measurements was very small (see Figure 6), yet we do not rule out that this can be more important in the future, with a possible expansion of the agricultural frontier within the $\Delta CO_{2_{obs}}$ footprint.

The differential response of vegetation within the seasonally-changing footprint is an important non-local driver of $\Delta CO_{2_{obs}}$ that is worth discussing further. We have already mentioned the findings of Castro et al. (2020) in which they showed substantial variability of SiF at the eco-region scale. However, within the ATTO eco-region the SiF reductions were not as large as those regionally, which is in contrast to the effect of the 2015/2016-El Niño on GPP at ATTO, which showed a notable reduction in 2015 (see Figure S5). This apparent discrepancy remains to be studied

further, however some plausible hypotheses are a non-linear behavior between SiF and GPP caused by extreme heat and drought (Martini, D. 2021 personal communication) in 2015 or that the GPP reduction observed at ATTO was a local phenomenon within the eco-region used in Castro et al. (2020). Nevertheless, Doughty et al. (2021) showed a linear relationship of GPP and SiF at different spatial scales, so the discrepancy of our eddy tower GPP with both SiF studies remains to be studied further.

Now, shifting to a more seasonal perspective, sites at the Tapajós National Forest (K67 and K83) and Caxiuanã (CAX) show a dry-season increase in GPP, which is driven by leaf age and not by seasonal LAI (Wu et al., 2016). It is interesting that at ATTO we observe this dry-season GPP increase on the mean seasonality, yet the amplitude of EC-NEE is different at all sites, being larger at the Tapajós sites followed by ATTO, CAX and K34 (Saleska et al., 2009). At the sites with larger EC-NEE amplitude, the role of R_{eco} modulating the EC-NEE is more important, which in turn is determined by the annual average rainfall as shown by Saleska et al. (2009). A further example of regional heterogeneity is given by the study of Restrepo-Coupe et al. (2013), in which they showed that sites where the dry season is very long or the soil is shallow, GPP does not increase during the dry season. This is the case for Rondônia, which has a long dry season similar to the Tapajós sites but with a shallow rocky soil, while Tapajós has deep soil which buffers the water available to plants (Nepstad et al., 2007).

The seasonal patterns of R_{eco} can be grouped into water-limited and oxygen-limited sites (Saleska et al., 2009). Water-limited sites, like the one in the Tapajós National forest (Saleska et al., 2003; Hutyra et al., 2007), exhibit dry season declines of R_{eco} as a result of an inhibited heterotrophic respiration due to a long dry season length that leads to the desiccation of decomposition sources near the surface (Saleska et al., 2003). The soil component of R_{eco} at oxygen-limited sites is inhibited with increasing soil moisture content, which is the case for K34 (Chambers et al., 2004). Our results suggest that the R_{eco} at ATTO follows an oxygen-limited regime with a MAP of 2383 mm yr^{-1} despite having a relatively long dry season length (3 months, see Table 1). Note that when including 2015 and 2016 in our analysis, R_{eco} does not show an increase in October, being suppressed during the dry season (see Figure 6). Therefore, the response of R_{eco} to disturbance at ATTO is in contrast to what was reported by Davidson et al. (2004) after a rainfall exclusion experiment for another site located on clay-dominated soil, where no significant effect was found.

One of the novelties of our study is the use of results from the recently-developed model (ORCHILEAK) for aquatic CO_2 evasion in Amazonia (Hastie et al., 2019) as an input in our atmospheric transport simulations. We have shown that the seasonal peak of $\Delta CO2_{obs}$ in June and July is influenced by a net carbon source driven by R_{eco} and the CO_2 evaded from rivers. The aquatic signal peaks in May and June (Figure 6), just when the $\Delta CO2_{obs}$ footprint covers the main branch of the Amazon River, including its delta (see MJJ in Figure 6 and 6). Therefore, we suggest that the $\Delta CO2_{obs}$ maximum in June has a larger contribution of CO_2 from rivers, while in July R_{eco} could be more relevant in the $\Delta CO2_{obs}$. We furthermore highlight that by adding aquatic CO_2 signals to FLUXCOM-$\Delta CO2_{sim}$: The shape of the seasonal cycle is closer to that of $\Delta CO2_{obs}$, indicating that aquatic CO_2 evasion is important to correctly represent the seasonal cycle of CO_2 mole fractions at ATTO.

A full error propagation from the river flux fields to our simulated tracer is out of the scope of this study. However, we provide an estimate for the relative error of about 35% for the river flux fields, which scales linearly to our simulated river signals. This estimate was based on Hastie et al., (2019), specifically the annual CO_2 evasion of 746 (526-998) Tg C per year. It is important to note that this relative error has to be interpreted with caution, as our atmospheric transport model (STILT) has a higher spatial resolution and the footprints do not cover the entire basin as the ORCHILEAK model does. This model represents an important advance in coupling the terrestrial carbon cycle with the lateral forest-river continuum, though the additional sources of uncertainty can be highlighted here. In ORCHILEAK the carbon sources of the CO_2 degassed from aquatic surfaces are attributed to: (1) dissolved organic carbon (DOC)

and dissolved CO_2 transported laterally from the upland soil and (2) decomposition of submerged organic carbon and litter and respiration of submerged roots in wetlands and rivers (see Lauerwald et al. (2017) and Lauerwald et al. (2020)). Lateral transport from upland soil (1) is important for small streams (Johnson et al., 2006, 2007), which are lacking in ORCHILEAK. In addition, the lack of aquatic plants in ORCHILEAK introduces uncertainty in (2). Including small streams and aquatic plants in ORCHILEAK would enable the model to better simulate CO_2 evasion from aquatic habitats.

5.2 | Fluxes are the major source of error in STILT simulations

Our study is the first to use the CO_2 ATTO record to independently evaluate optimized and non-optimized gridded NEE fluxes when transported in the atmosphere. From this evaluation we highlight two main important findings. The first is that none of the simulations, including the ones using optimized fluxes, accurately reproduce the seasonal cycle of the observed signal ($\Delta CO_{2_{obs}}$), which represents the regional flux and atmospheric transport influence. $\Delta CO_{2_{obs}}$ is almost always lower than the background inflow, indicating a sustained regional sink of CO_2. The second, is the importance of river CO_2 signals at ATTO when interpreting the CO_2 measurements and simulated biospheric signals. We showed that the phase of the seasonal cycle is better captured by FLUXCOM only when adding river signals (Figure 6), and that the amplitude of the seasonal cycle is overestimated by 0.8 ppm to 1.8 ppm (CT-SAM-Flask and VPRM).

We attribute the incapability of our system to accurately simulate $\Delta CO_{2_{obs}}$ mainly to errors in the input fluxes, which fail to capture the seasonal variability of NEE in the footprint area. Dynamic vegetation models are known to have difficulties simulating the seasonality of carbon fluxes in the equatorial (5°S to 5°N) band of Amazonia (Verbeeck et al., 2011; Restrepo-Coupe et al., 2017), but here we show that even when NEE of a process-based model (such as SiBCASA) is optimized with different data streams (using surface CO_2 observations CTE2020, additional aircraft profiles within the Amazonia CT-SAM-Flask and, satellite columns CT-SAM-OCO2), it does not capture the seasonality of $\Delta CO_{2_{obs}}$ sampled at ATTO. This finding is similar to that of Molina et al. (2015), in showing the difficulties of reproducing the seasonal cycle of NEE after an atmospheric inversion, but we further show the remaining challenges of a denser observational network, which could either be aircraft profiles (e.g., CT-SAM-Flask) within Amazonia or satellite columns (e.g., CT-SAM-OCO2). A still limited observational coverage, even with the aircraft network and the OCO2 columns, is perhaps one of the main remaining challenges.

The mismatch between the optimized fluxes and $\Delta CO_{2_{obs}}$ at inter-annual scale could be related to an incorrect seasonality in the prior NEE flux (i.e. NEE before optimization), but also to the frequency and spatial distribution of observations used in the assimilation. For CTE2020, CT-SAM-Flask and CT-SAM-OCO2 the same prior model is used (i.e. SiBCASA), but different data streams are assimilated. Tests indicate that the use of the same NEE prior leads to a similar shape of the seasonal cycle in the posterior NEE (not shown) and thus the $\Delta CO_{2_{sim}}$ in this study, regardless of the data assimilated for the optimization. Furthermore, the effects of temperature, soil moisture and precipitation anomalies in the underlying prior biosphere models (in particular for VPRM and SiBCASA) could produce inaccurate vegetation NEE responses in terms of timing and/or sign. This could result in NEE fluxes with either an early too strong source (i.e. 2015-NDJ) or the opposite in sign in the same month possibly due to an enhanced uptake (i.e., 2016-ASO).

This study is the first time that the FLUXCOM NEE product has been evaluated using atmospheric transport to obtain CO_2 mole fractions at a particular site in the tropics. Interestingly, we found similar inter-annual patterns in $\Delta CO_{2_{sim}}$ to those using the optimized fluxes, but not with the observations. Jung et al. (2020) found a consistency in NEE anomalies between FLUXCOM and atmospheric inversions at global scales, and here we show that this finding

holds at regional scales when using FLUXCOM in simulations of atmospheric CO_2. According to Jung et al. (2020), the reasons for the global consistency between FLUXCOM and atmospheric inversions are: 1. a spatial compensation of processes that are not well represented by the underlying model formulations and 2. the tendency of such models to be more sensitive to temperature signals, which are more important at larger spatial scales, as discussed in detail by Jung et al. (2017). Here we suggest that the spatial scale of our analysis can still suffer from the weaknesses listed above. In particular, note that the temperature sensitivity can be spotted by comparing Figures 6a and 6a; the bottom-up and top-down simulations converge in a 2σ anomaly in 2015-NDJ, coinciding with temperature anomalies of similar magnitude.

Inter-annual drought-induced impacts on vegetation in Amazonia can include: shifting carbon allocation from the canopy to fine roots following drought (Doughty et al., 2014), reduced growth due to water stress and warm temperatures (Clark et al., 2010), prioritizing growth at the expense of maintenance and defence (Doughty et al., 2015), and increased tree mortality (da Costa et al., 2010; Wang et al., 2012) together with reduced vegetation productivity (Feldpausch et al., 2016). In addition to the mechanisms listed above, the implementation of the different seasonal phenological stages (as shown in Figure 6 but also by Restrepo-Coupe et al. (2013), Lopes et al. (2016) and Wu et al. (2016)) needs to be improved in dynamic vegetation models as well as in process-based biosphere models, to produce more accurate NEE and thus $\Delta CO_{2_{sim}}$ estimates. Improving the sensitivity of tropical vegetation in dynamic vegetation models to water availability could also reduce the disagreement between top-down and bottom-up estimates for the global carbon budget (Bastos et al., 2020).

Atmospheric transport uncertainties are also a source of errors in our simulations, mainly associated with the model's capability to resolve moist (deep) convection (Betts et al., 2009), vertical mixing within the boundary layer (Gerbig et al., 2008) and advection (i.e., wind speed and wind direction) correctly. The seasonality of convection in STILT shows more activity during the wet season (FMA) over the footprint area, consistent with the timing of convective events reported by Horel et al. (1989). Therefore, the probability of a particle being captured by an updraft or downdraft is higher during the wet season. We are aware that errors in representing deep convection could lead to a potential bias in the turnover time of the air between the mid and upper troposphere and the boundary layer. We acknowledge this limitation, but if present, such a bias is more likely to occur in the wet season. STILT is as good as the driving meteorological fields and their ability to capture convective events. Convection is a sub-grid process that can impact the ability of Eulerian models to reproduce tracer transport at the mesoscale in Amazonia (Beck et al., 2013) and it can also be triggered by small scale processes (Burleyson et al., 2016), which present difficulties for their representation in atmospheric transport models. Thus, using higher spatial resolution driving fields, such as ERA5 (C3S, 2017), is expected to improve the model's representation of convection, as shown specifically for Lagrangian models by Hoffmann et al. (2019). To reduce vertical mixing errors, we filter both the STILT simulations and the observations, so as to obtain only afternoon values (13:00-17:00 LT) (see in Figure S4 the convergence of simulated and observed CO_2 in the afternoon).

Moreover, to evaluate advection errors at the receptor height (80 m), we compared local wind speed and direction measured at ATTO with the simulated quantities. We found a small bias in wind speed (-0.08 m s^{-1}) and a moderate bias in wind direction (-39 °). However, when evaluating directly the errors of the driving meteorological winds using three afternoon (14:00 LT) radiosondes at ATTO, we found that they decrease with height (Figure S9). This indicates that as the particle trajectories reach higher elevations, the error tends to decrease; the particle height after 2 days of back trajectory was on average 1400 m. A study using a Lagrangian model to evaluate the role of the Amazon Basin moisture in the hydrological cycle (Drumond et al., 2014) supports the orientation of the footprints shown here. Drumond et al. (2014) show that moisture sources in Amazonia during the austral summer are coming from the tropical North Atlantic Ocean, which is in line with our footprints for NDJ and FMA. Overall, given these findings, we conclude

that the errors in fluxes are much larger than those in transport.

6 | CONCLUSIONS AND OUTLOOK

In this study we presented and analysed the first six years of the CO_2 record from the Amazon Tall Tower Observatory. Using a Lagrangian atmospheric transport model we evaluated how well we could reproduce the observed CO_2 concentrations at ATTO. By combining atmospheric transport from STILT with a set of different NEE flux products, we found that the inversion results were not able to constrain the seasonal variability of $\Delta CO_{2_{obs}}$ in the footprint of the tower and very likely at the regional scale. It seems that the optimized products cannot adjust the prior seasonal cycle of NEE regardless of the data stream assimilated. Furthermore, we have presented evidence of the importance of river CO_2 evasion for getting the shape (but not the magnitude) of the seasonal cycle when using the FLUXCOM product, mainly capturing the increase in $\Delta CO_{2_{obs}}$ from May to July. We have further shown that the main controls of $\Delta CO_{2_{obs}}$ at seasonal and inter-annual scales result from the combined effect of local and non-local drivers, which can be inferred by the phase difference in EC-NEE and $\Delta CO_{2_{obs}}$.

This is not the first study to highlight the underlying processes that should be better represented in biosphere models, but it is the first evaluation of bottom-up and top-down NEE fluxes using an independent station with a long-term and continuous record in Amazonia. We therefore highlight the potential of the ATTO station, and the upcoming 325 m continuous record, as an independent validation site for atmospheric transport of CO_2 and for regional inversion estimates, which we are currently working on. Equally important are the seasonal patterns of carbon exchange, ecosystem respiration and leaf phenology that we have presented here, which add to the current body of literature (Saleska et al., 2003; von Randow et al., 2004; Hutyra et al., 2007; Baker et al., 2008; Restrepo-Coupe et al., 2013; Wu et al., 2016; Lopes et al., 2016) and provide in-situ information for constraining the heterogeneity of these processes in Amazonia. These findings are of utmost importance for regional carbon budget assessments, like the RECCAP2 initiative (`https://climate.esa.int/en/projects/reccap-2/`). By guiding the choice of prior fluxes to estimates with better NEE seasonality, improved posterior flux distributions and thus, regional carbon budgets, can be attained.

acknowledgements

This work and the ATTO project was funded by the German Federal Ministry of Education and Research (BMBF, contracts 01LB1001A and 01LK1602A) and supported by the International Max Planck Research School for Global Biogeochemical Cycles (IMPRS-gBGC). The ATTO project is furthermore funded by the Brazilian Ministério da Ciência, Tecnologia e Inovação (MCTI/FINEP contract 01.11.01248.00) and the Max Planck Society. We acknowledge the Instituto Nacional de Pesquisas da Amazonia as well as the Amazon State University (UEA), FAPEAM, LBA/INPA and SDS/CEUC/RDS-Uatumã for continuous support and logistical management. Many thanks to the people coordinating the scientific support at ATTO, in particular Susan Trumbore, Carlos Alberto Quesada, Bruno Takeshi, and Reiner Ditz. We want to thank all the personnel at the research site involved in technical and logistical support, especially Andrew Crozier, Stefan Wolff, Sam Jones, Leonardo Ramos de Oliveira, Nagib Alberto de Castro Souza, Roberta Pereira de Souza, Amauri Rodriguês Pereira, Hermes Braga Xavier, Wallace Rabelo Costa, Antonio Huxley Melo Nascimento, Uwe Schultz, Thomas Seifert, Steffen Schmidt and Thomas Disper. We express our gratitude to the data providers, Jessica Baker (Figure 1, underlying vegetation) and Rosa Santos (Radiosondes for evaluation), Sophia Walter and Martin Jung (FLUXCOM), Christian Roedenbeck (Jena Carboscope) and Ronny Lauerwald (river fluxes - ORCHILEAK). Many thanks

to John Melack for his fruitful comments about CO_2 river evasion measurements and regional estimates. Finally, we would like to acknowledge the two anonymous reviewers, whose comments improved the paper significantly. W.P. and G.K. were funded by an ERC-Consolidator grant (649087) as part of the ASICA (Airborne Stable Isotopes of Carbon from the Amazon) project.

conflict of interest

The authors declare no conflicts of interest.

Figure captions

Figure 1. The 50th and 75th percentiles for the seasonally averaged footprint for NDJ and FMA (left panel) and MJJ and ASO (right panel) overlain with the distribution of intact forest (dark green), non-intact forest (pale green), moderately deforested (pink) and severely deforested (magenta). Cerrado and Caatinga biomes are labeled but not coloured. The ATTO site is indicated with a red triangle. The distribution of vegetation state is taken from Baker and Spracklen (2019).

Figure 2. Monthly time series of the ATTO CO_2 measurements together with the simulated background concentrations without bias correction (continuous blue line) and with bias correction (dashed blue line) (a). The observed mole fractions at ATTO (measurement height 79 m) are shown in a thicker black line in (a) and the error bar represents $\pm$ 1 σ. The thin black line represents the linear trend fitted using the Theil-Sen slope. In (b) the seasonal cycle of the regional signal ($\Delta CO_{2_{obs}}$) is shown. The grey shading represents the min-max range given by the spread of the independent $\Delta CO_{2_{obs}}$, calculated using the interpolation between ASC and RPB, and the bias corrected $\Delta CO_{2_{obs}}$. To aggregate to monthly averages we selected only daytime values (i.e. 13:00-17:00 LT) to ensure well-mixed conditions in the PBL. The dry and wet seasons in (b) are the climatological seasons calculated with the TRMM dataset described in Section 3.1.

Figure 3. Mean seasonal cycle of the observed CO_2 regional signal $\Delta CO_{2_{obs}}$ and $\Delta CO_{2_{obs-bio}}$, together with monthly box-and-whisker plots of the eddy-covariance-derived NEE (EC-NEE) flux are shown in (a). Note that the EC-NEE includes the storage flux and the means are shown as triangles connected by a dotted line. Averaged seasonal cycles of Gross Primary Productivity (GPP) and ecosystem respiration (R_{eco}) (b) and, of Photosynthetic Active Radiation (PAR) together with the age classes of Leaf Area Index (LAI) (c). In (d) the monthly mean precipitation from the TRMM dataset (1998-2019), the STILT-simulated averaged seasonal signal of CO_2 [ppm] evasion from rivers (see Table 2 to see input fluxes used in STILT) and the Equivalent Water Height anomalies from the Gravity Recovery and Climate Experiment (GRACE) are shown (all available at: https://grace.jpl.nasa.gov/data-analysis-tool/. Last access: February 02, 2021). The area over which the GRACE data were integrated is marked with a purple square in the small inset on the lower right of (d). The markers in (a) and (b) are shifted to improve visibility and all the error bars represent the monthly standard deviation. The shaded areas in the background highlight the wet (Feb-Jun) and dry (Jul-Nov) seasons. The dry and wet seasons are the climatological seasons calculated with the TRMM dataset described in Section 3.1.

Figure 4. Standardized anomalies of $\Delta CO_{2_{obs-bio}}$, $\Delta CO_{2_{obs}}$ and EC-NEE (a) averaged over three-month periods, calculated against the 2014-2019 period, centered on the wet (FMA) and dry (ASO) seasons, with transition periods in between (MJJ and NDJ). The error bars denote the standard deviation for each season, calculated before aggregating to the seasonal mean. Thus, it shows the internal variation of each season for each year. In (b) the bi-monthly Multivariate El Niño index shows the strength of the El Niño event as measured by five different variables and aggregated in one index (data obtained from: https://psl.noaa.gov/enso/mei/; accessed on June 10, 2020), with values higher than 0.5 corresponding to a strong El Niño event. In the last panels, we show monthly standardized anomalies of air temperature at 81, 26 and 4 m and soil temperature at 20 and 40 cm (c), soil moisture at 10, 40 and 100 cm in (d) and precipitation (e). Soil moisture, air and soil temperature were measured at the ATTO site. Precipitation is taken from the TRMM dataset (1998-2019).

Figure 5. Seasonally-averaged concentration footprint (row a) for the inlet level of 80 m. These footprints were calculated with the output of hourly simulations of the STILT model covering the 2014-2019 time period. The first column in row (a) shows the regional context of the footprints and highlights the area shown in the rest of the panels. The ATTO site is indicated with a red marker. In the rest of the panels the location of the research site is indicated by the intersection of the parallel and meridian lines. NEE fluxes are shown in rows b to f.

Figure 6. Mean seasonal cycle of the regional signal for each of the simulated ($\Delta CO_{2_{sim}}$) and observed ($\Delta CO_{2_{obs}}$) mole fractions of CO_2. On the left panel the simulations using bottom-up NEE fluxes (i.e. VPRM and FLUXCOM) include the river signals. On the right panel river signals are not included in the bottom-up NEE fluxes, shown with a dashed line. The error bar in the observations represents $\pm$ 1 σ. For the simulated and observed mole fractions we selected only daytime values (i.e. 13:00-17:00 LT) to ensure well-mixed conditions in the PBL. The dry and wet seasons in are the climatological seasons calculated with the TRMM dataset described in Section 3.1.

Figure 7. Standardized anomalies of $\Delta CO_{2_{obs}}$ and the simulated tracers in STILT (a) averaged over three-month periods, calculated against the 2014-2019 period and centered on the wet (FMA) and dry (ASO) seasons, with transition periods in between (MJJ and NDJ). The error bars denote the standard deviation for each season, calculated before aggregating to the seasonal mean. Thus, it shows the internal variation of each season for each year. Note that CT-SAM-OCO2 is not shown here since we did not have enough simulated years to calculate an anomaly. The climatological standard deviation used for the standardization is shown in Figure **??**. The monthly contribution of simulated NEE, $\Delta CO_{2_{obs}}$ and $\Delta CO_{2_{bio}}$ is shown in (b). $\Delta CO_{2_{bio}}$ = $\Delta CO_{2_{obs}}$ - $(river, ff, fires, ocean)$. In (c), (d) and (e), the contribution of rivers, oceans and fires and fossil fuels are shown. Note the different scales on the y-axis.

Figure 8. Regional CO_2 signal ($\Delta CO_{2_{obs}}$) and EC-NEE averaged over non-ENSO years (2014, 2017-2019) (a) and ENSO years 2015-2016 (b). In (c) and (d) the same time periods are shown but for GPP and R_{eco}.

references

Albert, L. P., Wu, J., Prohaska, N., Camargo, P. B. d., Huxman, T. E., Tribuzy, E. S., Ivanov, V. Y., Oliveira, R. S., Garcia, S., Smith, M. N., Junior, R. C. O., Restrepo-Coupe, N., Silva, R. d., Stark, S. C., Martins, G. A., Penha, D. V. and Saleska, S. R. (2018) Age-dependent leaf physiology and consequences for crown-scale carbon uptake during the dry season in an Amazon evergreen forest. *New Phytologist*, **219**, 870–884.

Alden, C. B., Miller, J. B., Gatti, L. V., Gloor, M. M., Guan, K., Michalak, A. M., van der Laan-Luijkx, I. T., Touma, D., Andrews, A., Basso, L. S., Correia, C. S. C., Domingues, L. G., Joiner, J., Krol, M. C., Lyapustin, A. I., Peters, W., Shiga, Y. P., Thoning, K., van der Velde, I. R., van Leeuwen, T. T., Yadav, V. and Diffenbaugh, N. S. (2016) Regional atmospheric CO_2 inversion reveals seasonal and geographic differences in Amazon net biome exchange. *Global Change Biology*, **22**, 3427–3443.

Amaral, J. H. F., Melack, J. M., Barbosa, P. M., MacIntyre, S., Kasper, D., Cortés, A., Silva, T. S. F., Nunes de Sousa, R. and Forsberg, B. R. (2020) Carbon Dioxide Fluxes to the Atmosphere From Waters Within Flooded Forests in the Amazon Basin. *Journal of Geophysical Research: Biogeosciences*, **125**.

Andreae, M. O. (2001) The Biosphere: Pilot or Passenger on Spaceship Earth? In *Contributions to Global Change Research*, p59–66.

Andreae, M. O., Acevedo, O. C., Araùjo, A., Artaxo, P., Barbosa, C. G. G., Barbosa, H. M. J., Brito, J., Carbone, S., Chi, X., Cintra, B. B. L., da Silva, N. F., Dias, N. L., Dias-Júnior, C. Q., Ditas, F., Ditz, R., Godoi, A. F. L., Godoi, R. H. M., Heimann, M., Hoffmann, T., Kesselmeier, J., Könemann, T., Krüger, M. L., Lavric, J. V., Manzi, A. O., Lopes, A. P., Martins, D. L., Mikhailov, E. F., Moran-Zuloaga, D., Nelson, B. W., Nölscher, A. C., Santos Nogueira, D., Piedade, M. T. F., Pöhlker, C., Pöschl, U., Quesada, C. A., Rizzo, L. V., Ro, C.-U., Ruckteschler, N., Sá, L. D. A., de Oliveira Sá, M., Sales, C. B., dos Santos, R. M. N., Saturno, J., Schöngart, J., Sörgel, M., de Souza, C. M., de Souza, R. A. F., Su, H., Targhetta, N., Tóta, J., Trebs, I., Trumbore, S., van Eijck, A., Walter, D., Wang, Z., Weber, B., Williams, J., Winderlich, J., Wittmann, F., Wolff, S. and Yáñez-Serrano, A. M. (2015) The Amazon Tall Tower Observatory (ATTO): overview of pilot measurements on ecosystem ecology, meteorology, trace gases, and aerosols. *Atmospheric Chemistry and Physics*, **15**, 10723–10776.

Andreae, M. O., Artaxo, P., Beck, V., Bela, M., Freitas, S., Gerbig, C., Longo, K., Munger, J. W., Wiedemann, K. T. and Wofsy, S. C. (2012) Carbon monoxide and related trace gases and aerosols over the Amazon Basin during the wet and dry seasons. *Atmospheric Chemistry and Physics*, **12**, 6041–6065.

Aragão, L. E. O. C., Anderson, L. O., Fonseca, M. G., Rosan, T. M., Vedovato, L. B., Wagner, F. H., Silva, C. V. J., Junior, C. H. L. S., Arai, E., Aguiar, A. P., Barlow, J., Berenguer, E., Deeter, M. N., Domingues, L. G., Gatti, L., Gloor, M., Malhi, Y., Marengo, J. A., Miller, J. B., Phillips, O. L. and Saatchi, S. (2018) 21st Century drought-related fires counteract the decline of Amazon deforestation carbon emissions. *Nature Communications*, **9**, 1–12.

Baccini, A., Goetz, S. J., Walker, W. S., Laporte, N. T., Sun, M., Sulla-Menashe, D., Hackler, J., Beck, P. S. A., Dubayah, R., Friedl, M. A., Samanta, S. and Houghton, R. A. (2012) Estimated carbon dioxide emissions from tropical deforestation improved by carbon-density maps. *Nature Climate Change*, **2**, 182–185. Number: 3 Publisher: Nature Publishing Group.

Baker, I. T., Prihodko, L., Denning, A. S., Goulden, M., Miller, S. and Rocha, H. R. d. (2008) Seasonal drought stress in the Amazon: Reconciling models and observations. *Journal of Geophysical Research: Biogeosciences*, **113**.

Baker, J. C. A. and Spracklen, D. V. (2019) Climate Benefits of Intact Amazon Forests and the Biophysical Consequences of Disturbance. *Frontiers in Forests and Global Change*, **2**. Publisher: Frontiers.

Barlow, J., Berenguer, E., Carmenta, R. and França, F. (2020) Clarifying Amazonia's burning crisis. *Global Change Biology*, **26**, 319–321.

Bastos, A., O'Sullivan, M., Ciais, P., Makowski, D., Sitch, S., Friedlingstein, P., Chevallier, F., Rödenbeck, C., Pongratz, J., Luijkx, I. T., Patra, P. K., Peylin, P., Canadell, J. G., Lauerwald, R., Li, W., Smith, N. E., Peters, W., Goll, D. S., Jain, A., Kato, E., Lienert, S., Lombardozzi, D. L., Haverd, V., Nabel, J. E. M. S., Poulter, B., Tian, H., Walker, A. P. and Zaehle, S. (2020) Sources of Uncertainty in Regional and Global Terrestrial CO_2 Exchange Estimates. *Global Biogeochemical Cycles*, **34**.

Basu, S., Baker, D. F., Chevallier, F., Patra, P. K., Liu, J. and Miller, J. B. (2018) The impact of transport model differences on CO_2 surface flux estimates from OCO-2 retrievals of column average CO_2. *Atmospheric Chemistry and Physics*, **18**, 7189–7215. Publisher: Copernicus GmbH.

Beck, V., Gerbig, C., Koch, T., Bela, M. M., Longo, K. M., Freitas, S. R., Kaplan, J. O., Prigent, C., Bergamaschi, P. and Heimann, M. (2013) WRF-Chem simulations in the Amazon region during wet and dry season transitions: evaluation of methane models and wetland inundation maps. *Atmospheric Chemistry and Physics*, **13**, 7961–7982.

Betts, A. K., Fisch, G., von Randow, C., Silva Dias, M. A. F., Cohen, J. C. P., da Silva, R. and Fitzjarrald, D. R. (2009) The Amazonian boundary layer and mesoscale circulations. In *Geophysical Monograph Series* (eds. M. Keller, M. Bustamante, J. Gash and P. Silva Dias), vol. 186, 163–181. Washington, D. C.: American Geophysical Union.

Bodesheim, P., Jung, M., Gans, F., Mahecha, M. D. and Reichstein, M. (2018) Upscaled diurnal cycles of land–atmosphere fluxes: a new global half-hourly data product. *Earth System Science Data*, **10**, 1327–1365. Publisher: Copernicus GmbH.

Borchert, R., Calle, Z., Strahler, A. H., Baertschi, A., Magill, R. E., Broadhead, J. S., Kamau, J., Njoroge, J. and Muthuri, C. (2015) Insolation and photoperiodic control of tree development near the equator. *New Phytologist*, **205**, 7–13.

Botía, S., Gerbig, C., Marshall, J., Lavric, J. V., Walter, D., Pöhlker, C., Holanda, B., Fisch, G., Araújo, A. C. d., Sá, M. O., Teixeira, P. R., Resende, A. F., Dias-Junior, C. Q., Asperen, H. v., Oliveira, P. S., Stefanello, M. and Acevedo, O. C. (2020) Understanding nighttime methane signals at the Amazon Tall Tower Observatory (ATTO). *Atmospheric Chemistry and Physics*, **20**, 6583–6606. Publisher: Copernicus GmbH.

Brando, P. M., Goetz, S. J., Baccini, A., Nepstad, D. C., Beck, P. S. A. and Christman, M. C. (2010) Seasonal and interannual variability of climate and vegetation indices across the Amazon. *Proceedings of the National Academy of Sciences*, **107**, 14685–14690.

Brienen, R. J. W., Phillips, O. L., Feldpausch, T. R., Gloor, E., Baker, T. R., Lloyd, J., Lopez-Gonzalez, G., Monteagudo-Mendoza, A., Malhi, Y., Lewis, S. L., Vásquez Martinez, R., Alexiades, M., Álvarez Dávila, E., Alvarez-Loayza, P., Andrade, A., Aragão, L. E. O. C., Araujo-Murakami, A., Arets, E. J. M. M., Arroyo, L., Aymard C., G. A., Bánki, O. S., Baraloto, C., Barroso, J., Bonal, D., Boot, R. G. A., Camargo, J. L. C., Castilho, C. V., Chama, V., Chao, K. J., Chave, J., Comiskey, J. A., Cornejo Valverde, F., da Costa, L., de Oliveira, E. A., Di Fiore, A., Erwin, T. L., Fauset, S., Forsthofer, M., Galbraith, D. R., Grahame, E. S., Groot, N., Hérault, B., Higuchi, N., Honorio Coronado, E. N., Keeling, H., Killeen, T. J., Laurance, W. F., Laurance, S., Licona, J., Magnussen, W. E., Marimon, B. S., Marimon-Junior, B. H., Mendoza, C., Neill, D. A., Nogueira, E. M., Núñez, P., Pallqui Camacho, N. C., Parada, A., Pardo-Molina, G., Peacock, J., Peña-Claros, M., Pickavance, G. C., Pitman, N. C. A., Poorter, L., Prieto, A., Quesada, C. A., Ramírez, F., Ramírez-Angulo, H., Restrepo, Z., Roopsind, A., Rudas, A., Salomão, R. P., Schwarz, M., Silva, N., Silva-Espejo, J. E., Silveira, M., Stropp, J., Talbot, J., ter Steege, H., Teran-Aguilar, J., Terborgh, J., Thomas-Caesar, R., Toledo, M., Torello-Raventos, M., Umetsu, R. K., van der Heijden, G. M. F., van der Hout, P., Guimarães Vieira, I. C., Vieira, S. A., Vilanova, E., Vos, V. A. and Zagt, R. J. (2015) Long-term decline of the Amazon carbon sink. *Nature*, **519**, 344–348.

Burleyson, C. D., Feng, Z., Hagos, S. M., Fast, J., Machado, L. A. T. and Martin, S. T. (2016) Spatial Variability of the Background Diurnal Cycle of Deep Convection around the GoAmazon2014/5 Field Campaign Sites. *Journal of Applied Meteorology and Climatology*, **55**, 1579–1598.

C3S (2017) ERA5: Fifth generation of ECMWF atmospheric reanalyses of the global climate. URL: `https://cds.climate.copernicus.eu/cdsapp#!/home`.

Carneiro, R. G. and Fisch, G. (2020) Observational analysis of the daily cycle of the planetary boundary layer in the central Amazon during a non-El Niño year and El Niño year (GoAmazon project 2014/5). *Atmospheric Chemistry and Physics*, **20**, 5547–5558. Publisher: Copernicus GmbH.

Carvalhais, N., Forkel, M., Khomik, M., Bellarby, J., Jung, M., Migliavacca, M., u, M., Saatchi, S., Santoro, M., Thurner, M., Weber, U., Ahrens, B., Beer, C., Cescatti, A., Randerson, J. T. and Reichstein, M. (2014) Global covariation of carbon turnover times with climate in terrestrial ecosystems. *Nature*, **514**, 213–217.

Castro, A. O., Chen, J., Zang, C. S., Shekhar, A., Jimenez, J. C., Bhattacharjee, S., Kindu, M., Morales, V. H. and Rammig, A. (2020) OCO-2 Solar-Induced Chlorophyll Fluorescence Variability across Ecoregions of the Amazon Basin and the Extreme Drought Effects of El Niño (2015–2016). *Remote Sensing*, **12**, 1202. Number: 7 Publisher: Multidisciplinary Digital Publishing Institute.

Chambers, J. Q., Tribuzy, E. S., Toledo, L. C., Crispim, B. F., Higuchi, N., Santos, J. d., Araújo, A. C., Kruijt, B., Nobre, A. D. and Trumbore, S. E. (2004) Respiration from a Tropical Forest Ecosystem: Partitioning of Sources and Low Carbon Use Efficiency. *Ecological Applications*, **14**, 72–88.

Chen, X., Maignan, F., Viovy, N., Bastos, A., Goll, D., Wu, J., Liu, L., Yue, C., Peng, S., Yuan, W., Conceição, A. C. d., O'Sullivan, M. and Ciais, P. (2020) Novel Representation of Leaf Phenology Improves Simulation of Amazonian Evergreen Forest Photosynthesis in a Land Surface Model. *Journal of Advances in Modeling Earth Systems*, **12**.

Clark, D. B., Clark, D. A. and Oberbauer, S. F. (2010) Annual wood production in a tropical rain forest in NE Costa Rica linked to climatic variation but not to increasing CO2. *Global Change Biology*, **16**, 747–759.

da Costa, A. C. L., Galbraith, D., Almeida, S., Portela, B. T. T., da Costa, M., de Athaydes Silva Junior, J., Braga, A. P., de Gonçalves, P. H. L., de Oliveira, A. A., Fisher, R., Phillips, O. L., Metcalfe, D. B., Levy, P. and Meir, P. (2010) Effect of 7 yr of experimental drought on vegetation dynamics and biomass storage of an eastern Amazonian rainforest. *New Phytologist*, **187**, 579–591.

Crowell, S., Baker, D., Schuh, A., Basu, S., Jacobson, A. R., Chevallier, F., Liu, J., Deng, F., Feng, L., McKain, K., Chatterjee, A., Miller, J. B., Stephens, B. B., Eldering, A., Crisp, D., Schimel, D., Nassar, R., O'Dell, C. W., Oda, T., Sweeney, C., Palmer, P. I. and Jones, D. B. A. (2019) The 2015–2016 carbon cycle as seen from OCO-2 and the global in situ network. *Atmospheric Chemistry and Physics*, **19**, 9797–9831. Publisher: Copernicus GmbH.

Davidson, E. A., de Araújo, A. C., Artaxo, P., Balch, J. K., Brown, I. F., C. Bustamante, M. M., Coe, M. T., DeFries, R. S., Keller, M., Longo, M., Munger, J. W., Schroeder, W., Soares-Filho, B. S., Souza, C. M. and Wofsy, S. C. (2012) The Amazon basin in transition. *Nature*, **481**, 321–328.

Davidson, E. A., Ishida, F. Y. and Nepstad, D. C. (2004) Effects of an experimental drought on soil emissions of carbon dioxide, methane, nitrous oxide, and nitric oxide in a moist tropical forest. *Global Change Biology*, **10**, 718–730.

Devol, A. H., Forsberg, B. R., Richey, J. E. and Pimentel, T. P. (1995) Seasonal variation in chemical distributions in the Amazon (Solimões) River: A multiyear time series. *Global Biogeochemical Cycles*, **9**, 307–328.

Dlugokencky, E. and Tans, P. (2020) NOAA/GML, Trends in atmospheric carbon dioxide. URL: `www.esrl.noaa.gov/gmd/ccgg/trends/`.

Doughty, C. E., Malhi, Y., Araujo-Murakami, A., Metcalfe, D. B., Silva-Espejo, J. E., Arroyo, L., Heredia, J. P., Pardo-Toledo, E., Mendizabal, L. M., Rojas-Landivar, V. D., Vega-Martinez, M., Flores-Valencia, M., Sibler-Rivero, R., Moreno-Vare, L., Viscarra, L. J., Chuviru-Castro, T., Osinaga-Becerra, M. and Ledezma, R. (2014) Allocation trade-offs dominate the response of tropical forest growth to seasonal and interannual drought. *Ecology*, **95**, 2192–2201.

Doughty, C. E., Metcalfe, D. B., Girardin, C. A. J., Amézquita, F. F., Cabrera, D. G., Huasco, W. H., Silva-Espejo, J. E., Araujo-Murakami, A., da Costa, M. C., Rocha, W., Feldpausch, T. R., Mendoza, A. L. M., da Costa, A. C. L., Meir, P., Phillips, O. L. and Malhi, Y. (2015) Drought impact on forest carbon dynamics and fluxes in Amazonia. *Nature*, **519**, 78–82.

Doughty, R., Köhler, P., Frankenberg, C., Magney, T. S., Xiao, X., Qin, Y., Wu, X. and Moore, B. (2019) TROPOMI reveals dry-season increase of solar-induced chlorophyll fluorescence in the Amazon forest. *Proceedings of the National Academy of Sciences*, **116**, 22393–22398.

Doughty, R., Xiao, X., Qin, Y., Wu, X., Zhang, Y. and Moore, B. (2021) Small anomalies in dry-season greenness and chlorophyll fluorescence for Amazon moist tropical forests during El Niño and La Niña. *Remote Sensing of Environment*, **253**, 112196.

Drumond, A., Marengo, J., Ambrizzi, T., Nieto, R., Moreira, L. and Gimeno, L. (2014) The role of the Amazon Basin moisture in the atmospheric branch of the hydrological cycle: a Lagrangian analysis. *Hydrology and Earth System Sciences*, **18**, 2577–2598.

Feldpausch, T. R., Lloyd, J., Lewis, S. L., Brienen, R. J. W., Gloor, M., Monteagudo Mendoza, A., Lopez-Gonzalez, G., Banin, L., Abu Salim, K., Affum-Baffoe, K., Alexiades, M., Almeida, S., Amaral, I., Andrade, A., Aragão, L. E. O. C., Araujo Murakami, A., Arets, E. J. M. M., Arroyo, L., Aymard C., G. A., Baker, T. R., Bánki, O. S., Berry, N. J., Cardozo, N., Chave, J., Comiskey, J. A., Alvarez, E., de Oliveira, A., Di Fiore, A., Djagbletey, G., Domingues, T. F., Erwin, T. L., Fearnside, P. M., França, M. B., Freitas, M. A., Higuchi, N., E. Honorio C., Iida, Y., Jiménez, E., Kassim, A. R., Killeen, T. J., Laurance, W. F., Lovett, J. C., Malhi, Y., Marimon, B. S., Marimon-Junior, B. H., Lenza, E., Marshall, A. R., Mendoza, C., Metcalfe, D. J., Mitchard, E. T. A., Neill, D. A., Nelson, B. W., Nilus, R., Nogueira, E. M., Parada, A., Peh, K. S.-H., Pena Cruz, A., Peñuela, M. C., Pitman, N. C. A., Prieto, A., Quesada, C. A., Ramírez, F., Ramírez-Angulo, H., Reitsma, J. M., Rudas, A., Saiz, G., Salomão, R. P., Schwarz, M., Silva, N., Silva-Espejo, J. E., Silveira, M., Sonké, B., Stropp, J., Taedoumg, H. E., Tan, S., ter Steege, H., Terborgh, J., Torello-Raventos, M., van der Heijden, G. M. F., Vásquez, R., Vilanova, E., Vos, V. A., White, L., Willcock, S., Woell, H. and Phillips, O. L. (2012) Tree height integrated into pantropical forest biomass estimates. *Biogeosciences*, **9**, 3381–3403.

Feldpausch, T. R., Phillips, O. L., Brienen, R. J. W., Gloor, E., Lloyd, J., Lopez-Gonzalez, G., Monteagudo-Mendoza, A., Malhi, Y., Alarcón, A., Álvarez Dávila, E., Alvarez-Loayza, P., Andrade, A., Aragao, L. E. O. C., Arroyo, L., Aymard C., G. A., Baker, T. R., Baraloto, C., Barroso, J., Bonal, D., Castro, W., Chama, V., Chave, J., Domingues, T. F., Fauset, S., Groot, N., Honorio Coronado, E., Laurance, S., Laurance, W. F., Lewis, S. L., Licona, J. C., Marimon, B. S., Marimon-Junior, B. H., Mendoza Bautista, C., Neill, D. A., Oliveira, E. A., Oliveira dos Santos, C., Pallqui Camacho, N. C., Pardo-Molina, G., Prieto, A., Quesada, C. A., Ramírez, F., Ramírez-Angulo, H., Réjou-Méchain, M., Rudas, A., Saiz, G., Salomão, R. P., Silva-Espejo, J. E., Silveira, M., ter Steege, H., Stropp, J., Terborgh, J., Thomas-Caesar, R., van der Heijden, G. M. F., Vásquez Martinez, R., Vilanova, E. and Vos, V. A. (2016) Amazon forest response to repeated droughts. *Global Biogeochemical Cycles*, **30**, 964–982.

Fleischer, K., Rammig, A., De Kauwe, M. G., Walker, A. P., Domingues, T. F., Fuchslueger, L., Garcia, S., Goll, D. S., Grandis, A., Jiang, M., Haverd, V., Hofhansl, F., Holm, J. A., Kruijt, B., Leung, F., Medlyn, B. E., Mercado, L. M., Norby, R. J., Pak, B., von Randow, C., Quesada, C. A., Schaap, K. J., Valverde-Barrantes, O. J., Wang, Y.-P., Yang, X., Zaehle, S., Zhu, Q. and Lapola, D. M. (2019) Amazon forest response to CO 2 fertilization dependent on plant phosphorus acquisition. *Nature Geoscience*, **12**, 736–741. Number: 9 Publisher: Nature Publishing Group.

Forsberg, B. R., Melack, J. M., Richey, J. E. and Pimentel, T. P. (2017) Regional and seasonal variability in planktonic photosynthesis and planktonic community respiration in Amazon floodplain lakes. *Hydrobiologia*, **800**, 187–206. URL: https://doi.org/10.1007/s10750-017-3222-3.

Friedlingstein, P., O'Sullivan, M., Jones, M. W., Andrew, R. M., Hauck, J., Olsen, A., Peters, G. P., Peters, W., Pongratz, J., Sitch, S., Le Quéré, C., Canadell, J. G., Ciais, P., Jackson, R. B., Alin, S., Aragão, L. E. O. C., Arneth, A., Arora, V., Bates, N. R., Becker, M., Benoit-Cattin, A., Bittig, H. C., Bopp, L., Bultan, S., Chandra, N., Chevallier, F., Chini, L. P., Evans, W., Florentie, L., Forster, P. M., Gasser, T., Gehlen, M., Gilfillan, D., Gkritzalis, T., Gregor, L., Gruber, N., Harris, I., Hartung, K., Haverd, V., Houghton, R. A., Ilyina, T., Jain, A. K., Joetzjer, E., Kadono, K., Kato, E., Kitidis, V., Korsbakken, J. I., Landschützer, P., Lefèvre, N., Lenton, A., Lienert, S., Liu, Z., Lombardozzi, D., Marland, G., Metzl, N., Munro, D. R., Nabel, J. E. M. S., Nakaoka, S.-I., Niwa, Y., O'Brien, K., Ono, T., Palmer, P. I., Pierrot, D., Poulter, B., Resplandy, L., Robertson, E., Rödenbeck, C., Schwinger, J., Séférian, R., Skjelvan, I., Smith, A. J. P., Sutton, A. J., Tanhua, T., Tans, P. P., Tian, H., Tilbrook, B., van der Werf, G., Vuichard, N., Walker, A. P., Wanninkhof, R., Watson, A. J., Willis, D., Wiltshire, A. J., Yuan, W., Yue, X. and Zaehle, S. (2020) Global Carbon Budget 2020. *Earth System Science Data*, **12**, 3269–3340. Publisher: Copernicus GmbH.

Fu, R., Yin, L., Li, W., Arias, P. A., Dickinson, R. E., Huang, L., Chakraborty, S., Fernandes, K., Liebmann, B., Fisher, R. and Myneni, R. B. (2013) Increased dry-season length over southern Amazonia in recent decades and its implication for future climate projection. *Proceedings of the National Academy of Sciences*, **110**, 18110–18115.

Gatti, L. V., Gloor, M., Miller, J. B., Doughty, C. E., Malhi, Y., Domingues, L. G., Basso, L. S., Martinewski, A., Correia, C. S. C., Borges, V. F., Freitas, S., Braz, R., Anderson, L. O., Rocha, H., Grace, J., Phillips, O. L. and Lloyd, J. (2014) Drought sensitivity of Amazonian carbon balance revealed by atmospheric measurements. *Nature*, **506**, 76–80.

Gaubert, B., Stephens, B. B., Basu, S., Chevallier, F., Deng, F., Kort, E. A., Patra, P. K., Peters, W., Rödenbeck, C., Saeki, T., Schimel, D., Van der Laan-Luijkx, I., Wofsy, S. and Yin, Y. (2019) Global atmospheric CO_2 inverse models converging on neutral tropical land exchange, but disagreeing on fossil fuel and atmospheric growth rate. *Biogeosciences*, **16**, 117–134. Publisher: Copernicus GmbH.

Gerbig, C., Dolman, A. J. and Heimann, M. (2009) On observational and modelling strategies targeted at regional carbon exchange over continents. *Biogeosciences*, **6**, 1949–1959. Publisher: Copernicus GmbH.

Gerbig, C., Körner, S. and Lin, J. C. (2008) Vertical mixing in atmospheric tracer transport models: error characterization and propagation. *Atmospheric Chemistry and Physics*, **8**, 591–602. Publisher: Copernicus GmbH.

Gerbig, C., Lin, J. C., Wofsy, S. C., Daube, B. C., Andrews, A. E., Stephens, B. B., Bakwin, P. S. and Grainger, C. A. (2003) Toward constraining regional-scale fluxes of CO2 with atmospheric observations over a continent: 2. Analysis of COBRA data using a receptor-oriented framework. *Journal of Geophysical Research: Atmospheres*, **108**.

Gloor, M., Bakwin, P., Hurst, D., Lock, L., Draxler, R. and Tans, P. (2001) What is the concentration footprint of a tall tower? *Journal of Geophysical Research: Atmospheres*, **106**, 17831–17840.

Gloor, M., Barichivich, J., Ziv, G., Brienen, R., Schöngart, J., Peylin, P., Ladvocat Cintra, B. B., Feldpausch, T., Phillips, O. and Baker, J. (2015) Recent Amazon climate as background for possible ongoing and future changes of Amazon humid forests: AMAZON CLIMATE AND TROPICAL FORESTS. *Global Biogeochemical Cycles*, **29**, 1384–1399.

Gloor, M., Gatti, L., Brienen, R., Feldpausch, T. R., Phillips, O. L., Miller, J., Ometto, J. P., Rocha, H., Baker, T., de Jong, B., Houghton, R. A., Malhi, Y., Aragão, L. E. O. C., Guyot, J.-L., Zhao, K., Jackson, R., Peylin, P., Sitch, S., Poulter, B., Lomas, M., Zaehle, S., Huntingford, C., Levy, P. and Lloyd, J. (2012) The carbon balance of South America: a review of the status, decadal trends and main determinants. *Biogeosciences*, **9**, 5407–5430.

Gonçalves, N. B., Lopes, A. P., Dalagnol, R., Wu, J., Pinho, D. M. and Nelson, B. W. (2020) Both near-surface and satellite remote sensing confirm drought legacy effect on tropical forest leaf phenology after 2015/2016 ENSO drought. *Remote Sensing of Environment*, **237**, 111489.

Goulden, M. L., Miller, S. D., Rocha, H. R. d., Menton, M. C., Freitas, H. C. d., Figueira, A. M. e. S. and Sousa, C. A. D. d. (2004) Diel and Seasonal Patterns of Tropical Forest Co2 Exchange. *Ecological Applications*, **14**, 42–54.

Goulding, M., Barthem, R. and Ferreira, E. (2003) The Smithsonian atlas of the Amazon.

Green, J. K., Berry, J., Ciais, P., Zhang, Y. and Gentine, P. (2020) Amazon rainforest photosynthesis increases in response to atmospheric dryness. *Science Advances*, **6**.

Gurney, K. R., Law, R. M., Denning, A. S., Rayner, P. J., Baker, D., Bousquet, P., Bruhwiler, L., Chen, Y.-H., Ciais, P., Fan, S., Fung, I. Y., Gloor, M., Heimann, M., Higuchi, K., John, J., Maki, T., Maksyutov, S., Masarie, K., Peylin, P., Prather, M., Pak, B. C., Randerson, J., Sarmiento, J., Taguchi, S., Takahashi, T. and Yuen, C.-W. (2002) Towards robust regional estimates of CO 2 sources and sinks using atmospheric transport models. *Nature*, **415**, 626–630. Number: 6872 Publisher: Nature Publishing Group.

Hastie, A., Lauerwald, R., Ciais, P. and Regnier, P. (2019) Aquatic carbon fluxes dampen the overall variation of net ecosystem productivity in the Amazon basin: An analysis of the interannual variability in the boundless carbon cycle. *Global Change Biology*, **25**, 2094–2111.

Hayek, M. N., Longo, M., Wu, J., Smith, M. N., Restrepo-Coupe, N., Tapajós, R., da Silva, R., Fitzjarrald, D. R., Camargo, P. B., Hutyra, L. R., Alves, L. F., Daube, B., Munger, J. W., Wiedemann, K. T., Saleska, S. R. and Wofsy, S. C. (2018) Carbon exchange in an Amazon forest: from hours to years. *Biogeosciences*, **15**, 4833–4848.

Hess, L. L., Melack, J. M., Affonso, A. G., Barbosa, C., Gastil-Buhl, M. and Novo, E. M. L. M. (2015) Wetlands of the Lowland Amazon Basin: Extent, Vegetative Cover, and Dual-season Inundated Area as Mapped with JERS-1 Synthetic Aperture Radar. *Wetlands*, **35**, 745–756.

Hoffmann, L., Günther, G., Li, D., Stein, O., Wu, X., Griessbach, S., Heng, Y., Konopka, P., Müller, R., Vogel, B. and Wright, J. S. (2019) From ERA-Interim to ERA5: the considerable impact of ECMWF's next-generation reanalysis on Lagrangian transport simulations. *Atmospheric Chemistry and Physics*, **19**, 3097–3124.

Horel, J. D., Hahmann, A. N. and Geisler, J. E. (1989) An investigation of the Annual Cycle of Convective Activity over the Tropical Americas. *Journal of Climate*, **2**, 1388–1403. Publisher: American Meteorological Society Section: Journal of Climate.

Hu, L., Andrews, A. E., Thoning, K. W., Sweeney, C., Miller, J. B., Michalak, A. M., Dlugokencky, E., Tans, P. P., Shiga, Y. P., Mountain, M., Nehrkorn, T., Montzka, S. A., McKain, K., Kofler, J., Trudeau, M., Michel, S. E., Biraud, S. C., Fischer, M. L., Worthy, D. E. J., Vaughn, B. H., White, J. W. C., Yadav, V., Basu, S. and Velde, I. R. v. d. (2019) Enhanced North American carbon uptake associated with El Niño. *Science Advances*, **5**, eaaw0076.

Hubau, W., Lewis, S. L., Phillips, O. L., Affum-Baffoe, K., Beeckman, H., Cuní-Sanchez, A., Daniels, A. K., Ewango, C. E. N., Fauset, S., Mukinzi, J. M., Sheil, D., Sonké, B., Sullivan, M. J. P., Sunderland, T. C. H., Taedoumg, H., Thomas, S. C., White, L. J. T., Abernethy, K. A., Adu-Bredu, S., Amani, C. A., Baker, T. R., Banin, L. F., Baya, F., Begne, S. K., Bennett, A. C., Benedet, F., Bitariho, R., Bocko, Y. E., Boeckx, P., Boundja, P., Brienen, R. J. W., Brncic, T., Chezeaux, E., Chuyong, G. B., Clark, C. J., Collins, M., Comiskey, J. A., Coomes, D. A., Dargie, G. C., de Haulleville, T., Kamdem, M. N. D., Doucet, J.-L., Esquivel-Muelbert, A., Feldpausch, T. R., Fofanah, A., Foli, E. G., Gilpin, M., Gloor, E., Gonmadje, C., Gourlet-Fleury, S., Hall, J. S., Hamilton, A. C., Harris, D. J., Hart, T. B., Hockemba, M. B. N., Hladik, A., Ifo, S. A., Jeffery, K. J., Jucker, T., Yakusu, E. K., Kearsley, E., Kenfack, D., Koch, A., Leal, M. E., Levesley, A., Lindsell, J. A., Lisingo, J., Lopez-Gonzalez, G., Lovett, J. C., Makana, J.-R., Malhi, Y., Marshall, A. R., Martin, J., Martin, E. H., Mbayu, F. M., Medjibe, V. P., Mihindou, V., Mitchard, E. T. A., Moore, S., Munishi, P. K. T., Bengone, N. N., Ojo, L., Ondo, F. E., Peh, K. S.-H., Pickavance, G. C., Poulsen, A. D., Poulsen, J. R., Qie, L., Reitsma, J., Rovero, F., Swaine, M. D., Talbot, J., Taplin, J., Taylor, D. M., Thomas, D. W., Toirambe, B., Mukendi, J. T., Tuagben, D., Umunay, P. M., van der Heijden, G. M. F., Verbeeck, H., Vleminckx, J., Willcock, S., Wöll, H., Woods, J. T. and Zemagho, L. (2020) Asynchronous carbon sink saturation in African and Amazonian tropical forests. *Nature*, **579**, 80–87.

Huete, A., Didan, K., Shimabukuro, Y., Ratana, P., Saleska, S., Hutyra, L., Yang, W., Nemani, R. and Myneni, R. (2006) Amazon green-up with sunlight in dry season. *Geophysical Research Letters - GEOPHYS RES LETT*, **33**.

Huffman, C., Bolvin, D., Nelkin, E. and Adler, R. (2016) TRMM (TMPA) Precipitation L3 1 day 0.25 degree x 0.25 degree V7. Edited by Andrey Savtchenko, Goddard Earth Sciences Data and Information Services Center (GES DISC), Accessed: January 10, 2021. DOI: 10.5067/TRMM/TMPA/DAY/7.

Hutyra, L. R., Munger, J. W., Saleska, S. R., Gottlieb, E., Daube, B. C., Dunn, A. L., Amaral, D. F., Camargo, P. B. d. and Wofsy, S. C. (2007) Seasonal controls on the exchange of carbon and water in an Amazonian rain forest. *Journal of Geophysical Research: Biogeosciences*, **112**.

Janssens-Maenhout, G., Crippa, M., Guizzardi, D., Muntean, M., Schaaf, E., Dentener, F., Bergamaschi, P., Pagliari, V., Olivier, J. G. J., Peters, J. A. H. W., van Aardenne, J. A., Monni, S., Doering, U. and Petrescu, A. M. R. (2017) EDGAR v4.3.2 Global Atlas of the three major GreenhouseGas Emissions for the period 1970–2012. URL: `https://essd.copernicus.org/preprints/essd-2017-79/`.

Johnson, M. S., Lehmann, J., Couto, E. G., Filho, J. P. N. and Riha, S. J. (2006) DOC and DIC in Flowpaths of Amazonian Headwater Catchments with Hydrologically Contrasting Soils. *Biogeochemistry*, **81**, 45–57.

Johnson, M. S., Weiler, M., Couto, E. G., Riha, S. J. and Lehmann, J. (2007) Storm pulses of dissolved CO2 in a forested headwater Amazonian stream explored using hydrograph separation. *Water Resources Research*, **43**.

Jung, M., Henkel, K., Herold, M. and Churkina, G. (2006) Exploiting synergies of global land cover products for carbon cycle modeling. *Remote Sensing of Environment*, **101**, 534–553.

Jung, M., Reichstein, M., Schwalm, C. R., Huntingford, C., Sitch, S., Ahlström, A., Arneth, A., Camps-Valls, G., Ciais, P., Friedlingstein, P., Gans, F., Ichii, K., Jain, A. K., Kato, E., Papale, D., Poulter, B., Raduly, B., Rödenbeck, C., Tramontana, G., Viovy, N., Wang, Y.-P., Weber, U., Zaehle, S. and Zeng, N. (2017) Compensatory water effects link yearly global land CO 2 sink changes to temperature. *Nature*, **541**, 516–520.

Jung, M., Schwalm, C., Migliavacca, M., Walther, S., Camps-Valls, G., Koirala, S., Anthoni, P., Besnard, S., Bodesheim, P., Carvalhais, N., Chevallier, F., Gans, F., Goll, D. S., Haverd, V., Köhler, P., Ichii, K., Jain, A. K., Liu, J., Lombardozzi, D., Nabel, J. E. M. S., Nelson, J. A., O'Sullivan, M., Pallandt, M., Papale, D., Peters, W., Pongratz, J., Rödenbeck, C., Sitch, S., Tramontana, G., Walker, A., Weber, U. and Reichstein, M. (2020) Scaling carbon fluxes from eddy covariance sites to globe: synthesis and evaluation of the FLUXCOM approach. *Biogeosciences*, **17**, 1343–1365. Publisher: Copernicus GmbH.

Kaiser, J. W., Heil, A., Andreae, M. O., Benedetti, A., Chubarova, N., Jones, L., Morcrette, J.-J., Razinger, M., Schultz, M. G., Suttie, M. and van der Werf, G. R. (2012) Biomass burning emissions estimated with a global fire assimilation system based on observed fire radiative power. *Biogeosciences*, **9**, 527–554.

Kannenberg, S. A., Schwalm, C. R. and Anderegg, W. R. L. (2020) Ghosts of the past: how drought legacy effects shape forest functioning and carbon cycling. *Ecology Letters*, **23**, 891–901.

Keenan, T. F., Migliavacca, M., Papale, D., Baldocchi, D., Reichstein, M., Torn, M. and Wutzler, T. (2019) Widespread inhibition of daytime ecosystem respiration. *Nature Ecology & Evolution*, **3**, 407–415.

Khanna, J., Medvigy, D., Fueglistaler, S. and Walko, R. (2017) Regional dry-season climate changes due to three decades of Amazonian deforestation. *Nature Climate Change*, **7**, 200–204.

Kondo, M., Patra, P. K., Sitch, S., Friedlingstein, P., Poulter, B., Chevallier, F., Ciais, P., Canadell, J. G., Bastos, A., Lauerwald, R., Calle, L., Ichii, K., Anthoni, P., Arneth, A., Haverd, V., Jain, A. K., Kato, E., Kautz, M., Law, R. M., Lienert, S., Lombardozzi, D., Maki, T., Nakamura, T., Peylin, P., Rödenbeck, C., Zhuravlev, R., Saeki, T., Tian, H., Zhu, D. and Ziehn, T. (2020) State of the science in reconciling top-down and bottom-up approaches for terrestrial CO_2 budget. *Global Change Biology*, **26**, 1068–1084.

Koren, G. (2020) *Constraining the exchange of carbon dioxide over the Amazon: New insights from stable isotopes, remote sensing and inverse modeling*. Ph.D. thesis, Wageningen Univeristy. URL: `https://doi.org/10.18174/524771`.

Koren, G., van Schaik, E., Araújo, A. C., Boersma, K. F., Gärtner, A., Killaars, L., Kooreman, M. L., Kruijt, B., van der Laan-Luijkx, I. T., von Randow, C., Smith, N. E. and Peters, W. (2018) Widespread reduction in sun-induced fluorescence from the Amazon during the 2015/2016 El Niño. *Philosophical Transactions of the Royal Society B: Biological Sciences*, **373**, 20170408.

Kountouris, P., Gerbig, C., Rödenbeck, C., Karstens, U., Koch, T. F. and Heimann, M. (2018) Atmospheric CO_2 inversions on the mesoscale using data-driven prior uncertainties: quantification of the European terrestrial CO_2 fluxes. *Atmospheric Chemistry and Physics*, **18**, 3047–3064. Publisher: Copernicus GmbH.

Krol, M., Houweling, S., Bregman, B. and Bergamaschi, P. (2005) The two-way nested global chemistry-transport zoom model TM5: algorithm and applications. *Atmos. Chem. Phys.*, 16.

van der Laan-Luijkx, I. T., van der Velde, I. R., Krol, M. C., Gatti, L. V., Domingues, L. G., Correia, C. S. C., Miller, J. B., Gloor, M., van Leeuwen, T. T., Kaiser, J. W., Wiedinmyer, C., Basu, S., Clerbaux, C. and Peters, W. (2015) Response of the Amazon carbon balance to the 2010 drought derived with CarbonTracker South America. *Global Biogeochemical Cycles*, **29**, 1092–1108.

van der Laan-Luijkx, I. T., van der Velde, I. R., van der Veen, E., Tsuruta, A., Stanislawska, K., Babenhauserheide, A., Zhang, H. F., Liu, Y., He, W., Chen, H., Masarie, K. A., Krol, M. C. and Peters, W. (2017) The CarbonTracker Data Assimilation Shell (CTDAS) v1.0: implementation and global carbon balance 2001–2015. *Geoscientific Model Development*, **10**, 2785–2800.

Lasslop, G., Reichstein, M., Papale, D., Richardson, A. D., Arneth, A., Barr, A., Stoy, P. and Wohlfahrt, G. (2010) Separation of net ecosystem exchange into assimilation and respiration using a light response curve approach: critical issues and global evaluation. *Global Change Biology*, **16**, 187–208.

Lauerwald, R., Regnier, P., Camino-Serrano, M., Guenet, B., Guimberteau, M., Ducharne, A., Polcher, J. and Ciais, P. (2017) ORCHILEAK (revision 3875): a new model branch to simulate carbon transfers along the terrestrial–aquatic continuum of the Amazon basin. *Geoscientific Model Development*, **10**, 3821–3859. Publisher: Copernicus GmbH.

Lauerwald, R., Regnier, P., Guenet, B., Friedlingstein, P. and Ciais, P. (2020) How Simulations of the Land Carbon Sink Are Biased by Ignoring Fluvial Carbon Transfers: A Case Study for the Amazon Basin. *One Earth*, **3**, 226–236. Publisher: Elsevier.

Lin, J. C., Gerbig, C., Wofsy, S. C., Andrews, A. E., Daube, B., Davis, K. and Grainger, C. A. (2003) A near-field tool for simulating the upstream influence of atmospheric observations: The Stochastic Time-Inverted Lagrangian Transport (STILT) model. *Journal of Geophysical Research*, **108**, ACH 2–1–ACH 2–17.

Liu, J., Bowman, K. W., Schimel, D. S., Parazoo, N. C., Jiang, Z., Lee, M., Bloom, A. A., Wunch, D., Frankenberg, C., Sun, Y., O'Dell, C. W., Gurney, K. R., Menemenlis, D., Gierach, M., Crisp, D. and Eldering, A. (2017) Contrasting carbon cycle responses of the tropical continents to the 2015–2016 El Niño. *Science*, **358**.

Lopes, A. P., Nelson, B. W., Wu, J., Graça, P. M. L. d. A., Tavares, J. V., Prohaska, N., Martins, G. A. and Saleska, S. R. (2016) Leaf flush drives dry season green-up of the Central Amazon. *Remote Sensing of Environment*, **182**, 90–98.

Mahadevan, P., Wofsy, S. C., Matross, D. M., Xiao, X., Dunn, A. L., Lin, J. C., Gerbig, C., Munger, J. W., Chow, V. Y. and Gottlieb, E. W. (2008) A satellite-based biosphere parameterization for net ecosystem CO2 exchange: Vegetation Photosynthesis and Respiration Model (VPRM). *Global Biogeochemical Cycles*, **22**.

Malhi, Y., Doughty, C. E., Goldsmith, G. R., Metcalfe, D. B., Girardin, C. A. J., Marthews, T. R., del Aguila-Pasquel, J., Aragão, L. E. O. C., Araujo-Murakami, A., Brando, P., da Costa, A. C. L., Silva-Espejo, J. E., Farfán Amézquita, F., Galbraith, D. R., Quesada, C. A., Rocha, W., Salinas-Revilla, N., Silvério, D., Meir, P. and Phillips, O. L. (2015) The linkages between photosynthesis, productivity, growth and biomass in lowland Amazonian forests. *Global Change Biology*, **21**, 2283–2295.

Malhi, Y., Rowland, L., Aragão, L. E. O. C. and Fisher, R. A. (2018) New insights into the variability of the tropical land carbon cycle from the El Niño of 2015/2016. *Philosophical Transactions of the Royal Society B: Biological Sciences*, **373**, 20170298. Publisher: Royal Society.

Malhi, Y., Wood, D., Baker, T. R., Wright, J., Phillips, O. L., Cochrane, T., Meir, P., Chave, J., Almeida, S., Arroyo, L., Higuchi, N., Killeen, T. J., Laurance, S. G., Laurance, W. F., Lewis, S. L., Monteagudo, A., Neill, D. A., Vargas, P. N., Pitman, N. C. A., Quesada, C. A., Salomao, R., Silva, J. N. M., Lezama, A. T., Terborgh, J., Martinez, R. V. and Vinceti, B. (2006) The regional variation of aboveground live biomass in old-growth Amazonian forests. *Global Change Biology*, **12**, 1107–1138.

Marengo, J. A. and Espinoza, J. C. (2016) Extreme seasonal droughts and floods in Amazonia: causes, trends and impacts. *International Journal of Climatology*, **36**, 1033–1050.

Mauder, M. and Foken, T. (2004) Documentation and Instruction Manual of the Eddy Covariance Software Package TK2.

Mitchard, E. T. A. (2018) The tropical forest carbon cycle and climate change. *Nature*, **559**, 527–534.

Molina, L., Broquet, G., Imbach, P., Chevallier, F., Poulter, B., Bonal, D., Burban, B., Ramonet, M., Gatti, L. V., Wofsy, S. C., Munger, J. W., Dlugokencky, E. and Ciais, P. (2015) On the ability of a global atmospheric inversion to constrain variations of CO2 fluxes over Amazonia. *Atmospheric Chemistry and Physics*, **15**, 8423–8438.

Myneni, R. B., Yang, W., Nemani, R. R., Huete, A. R., Dickinson, R. E., Knyazikhin, Y., Didan, K., Fu, R., Juárez, R. I. N., Saatchi, S. S., Hashimoto, H., Ichii, K., Shabanov, N. V., Tan, B., Ratana, P., Privette, J. L., Morisette, J. T., Vermote, E. F., Roy, D. P., Wolfe, R. E., Friedl, M. A., Running, S. W., Votava, P., El-Saleous, N., Devadiga, S., Su, Y. and Salomonson, V. V. (2007) Large seasonal swings in leaf area of Amazon rainforests. *Proceedings of the National Academy of Sciences*, **104**, 4820–4823.

Nehrkorn, T., Eluszkiewicz, J., Wofsy, S. C., Lin, J. C., Gerbig, C., Longo, M. and Freitas, S. (2010) Coupled weather research and forecasting–stochastic time-inverted lagrangian transport (WRF–STILT) model. *Meteorology and Atmospheric Physics*, **107**, 51–64.

Nepstad, D. C., Tohver, I. M., Ray, D., Moutinho, P. and Cardinot, G. (2007) Mortality of Large Trees and Lianas Following Experimental Drought in an Amazon Forest. *Ecology*, **88**, 2259–2269.

Papale, D., Reichstein, M., Aubinet, M., Canfora, E., Bernhofer, C., Kutsch, W., Longdoz, B., Rambal, S., Valentini, R., Vesala, T. and Yakir, D. (2006) Towards a standardized processing of Net Ecosystem Exchange measured with eddy covariance technique: algorithms and uncertainty estimation. *Biogeosciences*, **3**, 571–583.

Peters, W., Jacobson, A. R., Sweeney, C., Andrews, A. E., Conway, T. J., Masarie, K., Miller, J. B., Bruhwiler, L. M. P., Petron, G., Hirsch, A. I., Worthy, D. E. J., van der Werf, G. R., Randerson, J. T., Wennberg, P. O., Krol, M. C. and Tans, P. P. (2007) An atmospheric perspective on North American carbon dioxide exchange: CarbonTracker. *Proceedings of the National Academy of Sciences*, **104**, 18925–18930.

Peters, W., Miller, J. B., Whitaker, J., Denning, A. S., Hirsch, A., Krol, M. C., Zupanski, D., Bruhwiler, L. and Tans, P. P. (2005) An ensemble data assimilation system to estimate CO $_2$ surface fluxes from atmospheric trace gas observations. *Journal of Geophysical Research*, **110**.

Peylin, P., Law, R. M., Gurney, K. R., Chevallier, F., Jacobson, A. R., Maki, T., Niwa, Y., Patra, P. K., Peters, W., Rayner, P. J., Rödenbeck, C., van der Laan-Luijkx, I. T. and Zhang, X. (2013) Global atmospheric carbon budget: results from an ensemble of atmospheric CO_2 inversions. *Biogeosciences*, **10**, 6699–6720. Publisher: Copernicus GmbH.

Pöhlker, C., Walter, D., Paulsen, H., Könemann, T., Rodríguez-Caballero, E., Moran-Zuloaga, D., Brito, J., Carbone, S., Degrendele, C., Després, V. R., Ditas, F., Holanda, B. A., Kaiser, J. W., Lammel, G., Lavrič, J. V., Ming, J., Pickersgill, D., Pöhlker, M. L., Praß, M., Löbs, N., Saturno, J., Sörgel, M., Wang, Q., Weber, B., Wolff, S., Artaxo, P., Pöschl, U. and Andreae, M. O. (2019) Land cover and its transformation in the backward trajectory footprint region of the Amazon Tall Tower Observatory. *Atmospheric Chemistry and Physics*, **19**, 8425–8470.

von Randow, C., Manzi, A. O., Kruijt, B., de Oliveira, P. J., Zanchi, F. B., Silva, R. L., Hodnett, M. G., Gash, J. H. C., Elbers, J. A., Waterloo, M. J., Cardoso, F. L. and Kabat, P. (2004) Comparative measurements and seasonal variations in energy and carbon exchange over forest and pasture in South West Amazonia. *Theoretical and Applied Climatology*, **78**, 5–26. URL: `https://doi.org/10.1007/s00704-004-0041-z`.

von Randow, C., Zeri, M., Restrepo-Coupe, N., Muza, M. N., de Gonçalves, L. G. G., Costa, M. H., Araujo, A. C., Manzi, A. O., da Rocha, H. R., Saleska, S. R., Arain, M. A., Baker, I. T., Cestaro, B. P., Christoffersen, B., Ciais, P., Fisher, J. B., Galbraith, D., Guan, X., van den Hurk, B., Ichii, K., Imbuzeiro, H., Jain, A., Levine, N., Miguez-Macho, G., Poulter, B., Roberti, D. R., Sahoo, A., Schaefer, K., Shi, M., Tian, H., Verbeeck, H. and Yang, Z.-L. (2013) Inter-annual variability of carbon and water fluxes in Amazonian forest, Cerrado and pasture sites, as simulated by terrestrial biosphere models. *Agricultural and Forest Meteorology*, **182-183**, 145–155.

Reichstein, M., Falge, E., Baldocchi, D., Papale, D., Aubinet, M., Berbigier, P., Bernhofer, C., Buchmann, N., Gilmanov, T., Granier, A., Grünwald, T., Havránková, K., Ilvesniemi, H., Janous, D., Knohl, A., Laurila, T., Lohila, A., Loustau, D., Matteucci, G., Meyers, T., Miglietta, F., Ourcival, J.-M., Pumpanen, J., Rambal, S., Rotenberg, E., Sanz, M., Tenhunen, J., Seufert, G., Vaccari, F., Vesala, T., Yakir, D. and Valentini, R. (2005) On the separation of net ecosystem exchange into assimilation and ecosystem respiration: review and improved algorithm. *Global Change Biology*, **11**, 1424–1439.

Restrepo-Coupe, N., da Rocha, H. R., Hutyra, L. R., da Araujo, A. C., Borma, L. S., Christoffersen, B., Cabral, O. M., de Camargo, P. B., Cardoso, F. L., da Costa, A. C. L., Fitzjarrald, D. R., Goulden, M. L., Kruijt, B., Maia, J. M., Malhi, Y. S., Manzi, A. O., Miller, S. D., Nobre, A. D., von Randow, C., Sá, L. D. A., Sakai, R. K., Tota, J., Wofsy, S. C., Zanchi, F. B. and Saleska, S. R. (2013) What drives the seasonality of photosynthesis across the Amazon basin? A cross-site analysis of eddy flux tower measurements from the Brasil flux network. *Agricultural and Forest Meteorology*, **182-183**, 128–144.

Restrepo-Coupe, N., Levine, N. M., Christoffersen, B. O., Albert, L. P., Wu, J., Costa, M. H., Galbraith, D., Imbuzeiro, H., Martins, G., Araujo, A. C. d., Malhi, Y. S., Zeng, X., Moorcroft, P. and Saleska, S. R. (2017) Do dynamic global vegetation models capture the seasonality of carbon fluxes in the Amazon basin? A data-model intercomparison. *Global Change Biology*, **23**, 191–208.

Richey, J. E., Melack, J. M., Aufdenkampe, A. K., Ballester, V. M. and Hess, L. L. (2002) Outgassing from Amazonian rivers and wetlands as a large tropical source of atmospheric CO2. *Nature*, **416**, 617–620.

Rödenbeck, C., Houweling, S., Gloor, M. and Heimann, M. (2003) CO2 flux history 1982–2001 inferred from atmospheric data using a global inversion of atmospheric transport. *Atmos. Chem. Phys.*, 46.

Saatchi, S. S., Houghton, R. A., Alvalá, R. C. D. S., Soares, J. V. and Yu, Y. (2007) Distribution of aboveground live biomass in the Amazon basin. *Global Change Biology*, **13**, 816–837.

Saleska, S., Rocha, H. R. d., Kruijt, B. and Nobre, A. D. (2009) Changes in Amazonian forest biomass, dynamics, and composition, 1980–2002. In *Geophysical Monograph Series* (eds. M. Keller, M. Bustamante, J. Gash and P. Silva Dias), vol. 186, 373–387. Washington, D. C.: American Geophysical Union.

Saleska, S. R., Miller, S. D., Matross, D. M., Goulden, M. L., Wofsy, S. C., Rocha, H. R. d., Camargo, P. B. d., Crill, P., Daube, B. C., Freitas, H. C. d., Hutyra, L., Keller, M., Kirchhoff, V., Menton, M., Munger, J. W., Pyle, E. H., Rice, A. H. and Silva, H. (2003) Carbon in Amazon Forests: Unexpected Seasonal Fluxes and Disturbance-Induced Losses. *Science*, **302**, 1554–1557.

Schaefer, K., Collatz, G. J., Tans, P., Denning, A. S., Baker, I., Berry, J., Prihodko, L., Suits, N. and Philpott, A. (2008) Combined Simple Biosphere/Carnegie-Ames-Stanford Approach terrestrial carbon cycle model. *Journal of Geophysical Research*, **113**.

van Schaik, E., Killaars, L., Smith, N. E., Koren, G., van Beek, L. P. H., Peters, W. and van der Laan-Luijkx, I. T. (2018) Changes in surface hydrology, soil moisture and gross primary production in the Amazon during the 2015/2016 El Niño. *Philosophical Transactions of the Royal Society B: Biological Sciences*, **373**, 20180084.

Schuh, A. E., Denning, A. S., Corbin, K. D., Baker, I. T., Uliasz, M., Parazoo, N., Andrews, A. E. and Worthy, D. E. J. (2010) A regional high-resolution carbon flux inversion of North America for 2004. *Biogeosciences*, **7**, 1625–1644. Publisher: Copernicus GmbH.

Shiga, Y. P., Michalak, A. M., Fang, Y., Schaefer, K., Andrews, A. E., Huntzinger, D. H., Schwalm, C. R., Thoning, K. and Wei, Y. (2018) Forests dominate the interannual variability of the North American carbon sink. *Environmental Research Letters*, **13**, 084015. Publisher: IOP Publishing.

Sitch, S., Friedlingstein, P., Gruber, N., Jones, S. D., Murray-Tortarolo, G., Ahlström, A., Doney, S. C., Graven, H., Heinze, C., Huntingford, C., Levis, S., Levy, P. E., Lomas, M., Poulter, B., Viovy, N., Zaehle, S., Zeng, N., Arneth, A., Bonan, G., Bopp, L., Canadell, J. G., Chevallier, F., Ciais, P., Ellis, R., Gloor, M., Peylin, P., Piao, S. L., Le Quéré, C., Smith, B., Zhu, Z. and Myneni, R. (2015) Recent trends and drivers of regional sources and sinks of carbon dioxide. *Biogeosciences*, **12**, 653–679. Publisher: Copernicus GmbH.

Thompson, R. L., Patra, P. K., Chevallier, F., Maksyutov, S., Law, R. M., Ziehn, T., van der Laan-Luijkx, I. T., Peters, W., Ganshin, A., Zhuravlev, R., Maki, T., Nakamura, T., Shirai, T., Ishizawa, M., Saeki, T., Machida, T., Poulter, B., Canadell, J. G. and Ciais, P. (2016) Top–down assessment of the Asian carbon budget since the mid 1990s. *Nature Communications*, **7**, 10724. Number: 1 Publisher: Nature Publishing Group.

Tiedtke, M. (1989) A Comprehensive Mass Flux Scheme for Cumulus Parameterization in Large-Scale Models. *Monthly Weather Review*, **117**, 1779–1800. Publisher: American Meteorological Society.

Verbeeck, H., Peylin, P., Bacour, C., Bonal, D., Steppe, K. and Ciais, P. (2011) Seasonal patterns of CO_2 fluxes in Amazon forests: Fusion of eddy covariance data and the ORCHIDEE model. *Journal of Geophysical Research*, **116**, G02018.

Vickers, D. and Mahrt, L. (1997) Quality Control and Flux Sampling Problems for Tower and Aircraft Data. *Journal of Atmospheric and Oceanic Technology*, **14**, 512–526.

Wang, W., Peng, C., Kneeshaw, D., Larocque, G. and Luo, Z.-B. (2012) Drought-induced tree mortality: Ecological consequences, causes, and modeling. *Environmental Reviews*, **20**, 109–121.

van der Werf, G. R., Randerson, J. T., Giglio, L., Collatz, G. J., Mu, M., Kasibhatla, P. S., Morton, D. C., DeFries, R. S., Jin, Y. and van Leeuwen, T. T. (2010) Global fire emissions and the contribution of deforestation, savanna, forest, agricultural, and peat fires (1997–2009). *Atmos. Chem. Phys.*, **10**, 11707–11735.

Wigneron, J.-P., Fan, L., Ciais, P., Bastos, A., Brandt, M., Chave, J., Saatchi, S., Baccini, A. and Fensholt, R. (2020) Tropical forests did not recover from the strong 2015–2016 El Niño event. *Science Advances*, **6**.

Winderlich, J., Chen, H., Gerbig, C., Seifert, T., Kolle, O., Lavrič, J. V., Kaiser, C., Höfer, A. and Heimann, M. (2010) Continuous low-maintenance $CO_2/CH_4/H_2O$ measurements at the Zotino Tall Tower Observatory (ZOTTO) in Central Siberia. *Atmospheric Measurement Techniques*, **3**, 1113–1128.

Winderlich, J., Gerbig, C., Kolle, O. and Heimann, M. (2014) Inferences from CO_2 and CH_4 concentration profiles at the Zotino Tall Tower Observatory (ZOTTO) on regional summertime ecosystem fluxes. *Biogeosciences*, **11**, 2055–2068. Publisher: Copernicus GmbH.

Wu, J., Albert, L. P., Lopes, A. P., Restrepo-Coupe, N., Hayek, M., Wiedemann, K. T., Guan, K., Stark, S. C., Christoffersen, B., Prohaska, N., Tavares, J. V., Marostica, S., Kobayashi, H., Ferreira, M. L., Campos, K. S., Silva, R. d., Brando, P. M., Dye, D. G., Huxman, T. E., Huete, A. R., Nelson, B. W. and Saleska, S. R. (2016) Leaf development and demography explain photosynthetic seasonality in Amazon evergreen forests. *Science*, **351**, 972–976.

Wutzler, T., Lucas-Moffat, A., Migliavacca, M., Knauer, J., Sickel, K., Šigut, L., Menzer, O. and Reichstein, M. (2018) Basic and extensible post-processing of eddy covariance flux data with REddyProc. *Biogeosciences*, **15**, 5015–5030. Publisher: Copernicus GmbH.

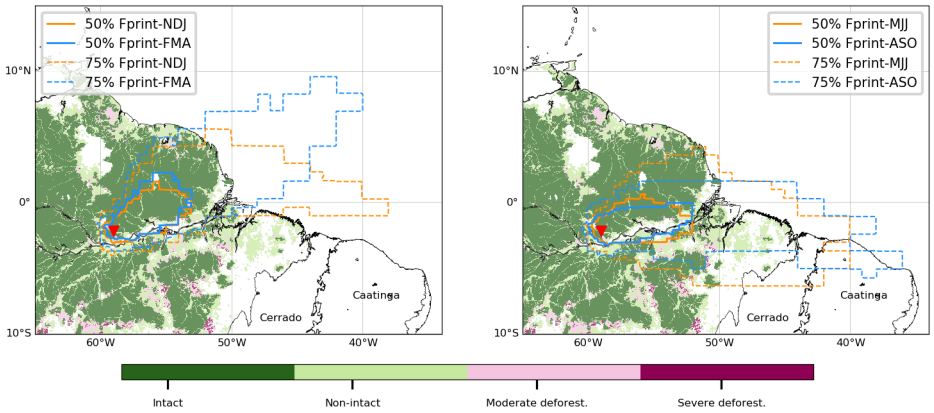

gcb_15905_f1.png

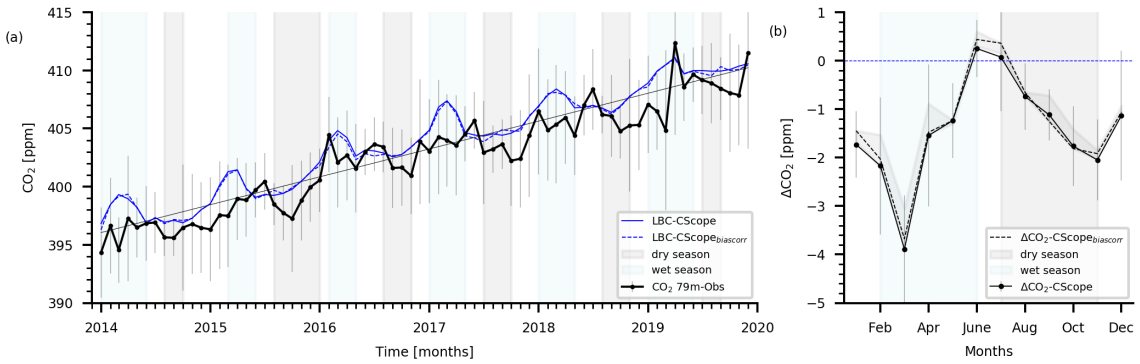

gcb_15905_f2.png

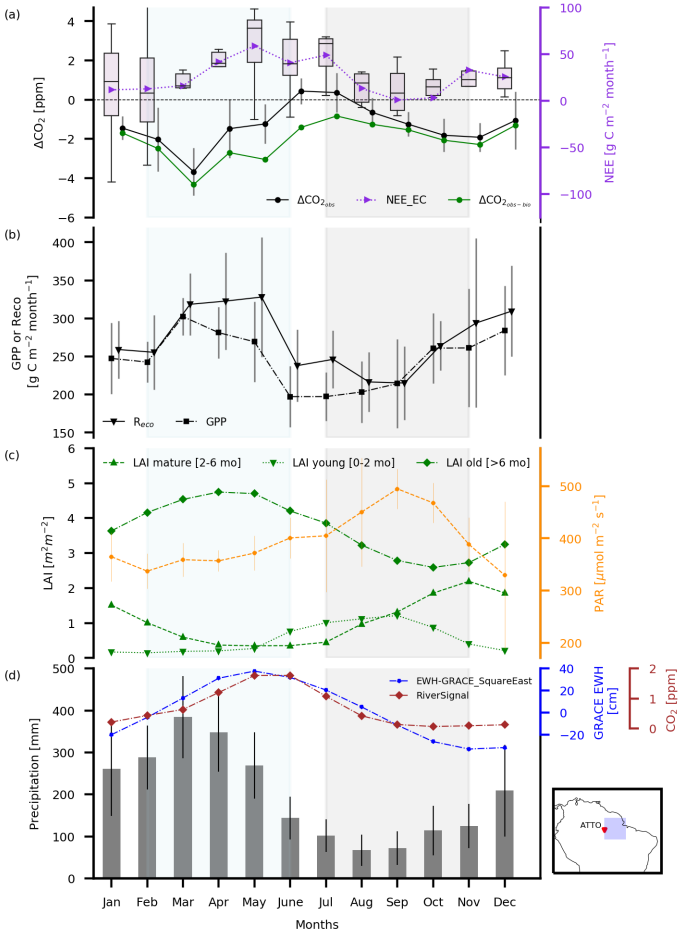

gcb_15905_f3.png

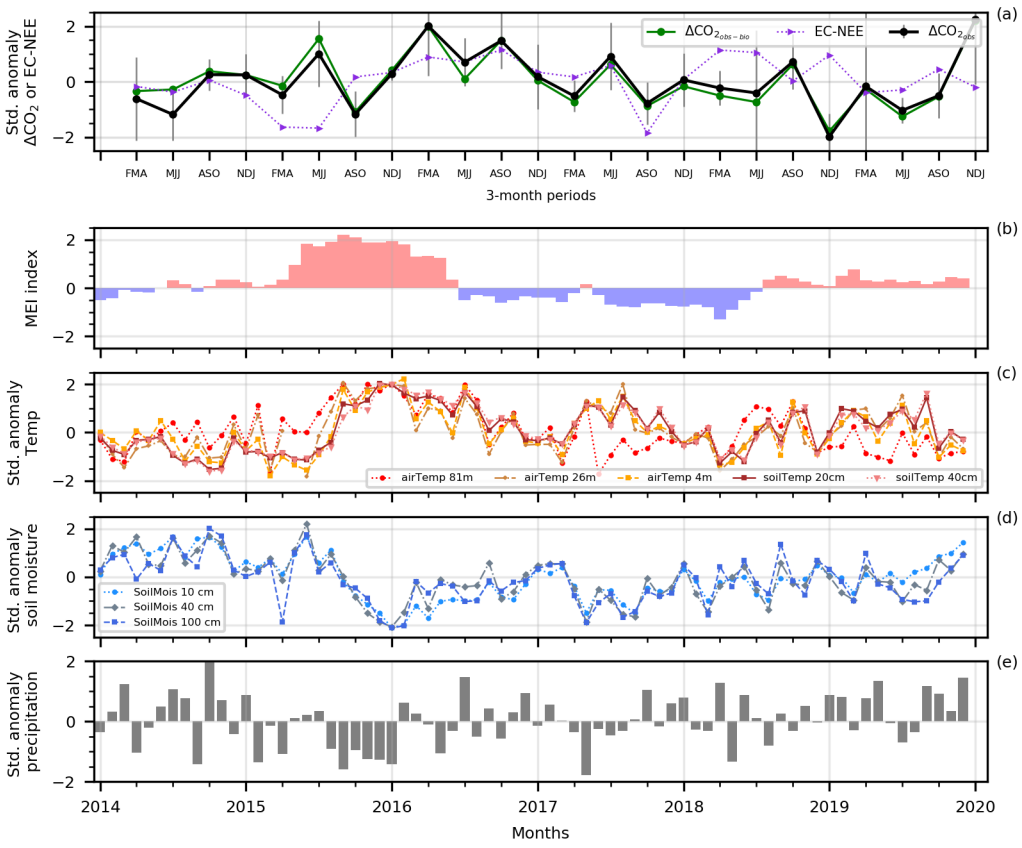

gcb_15905_f4.png

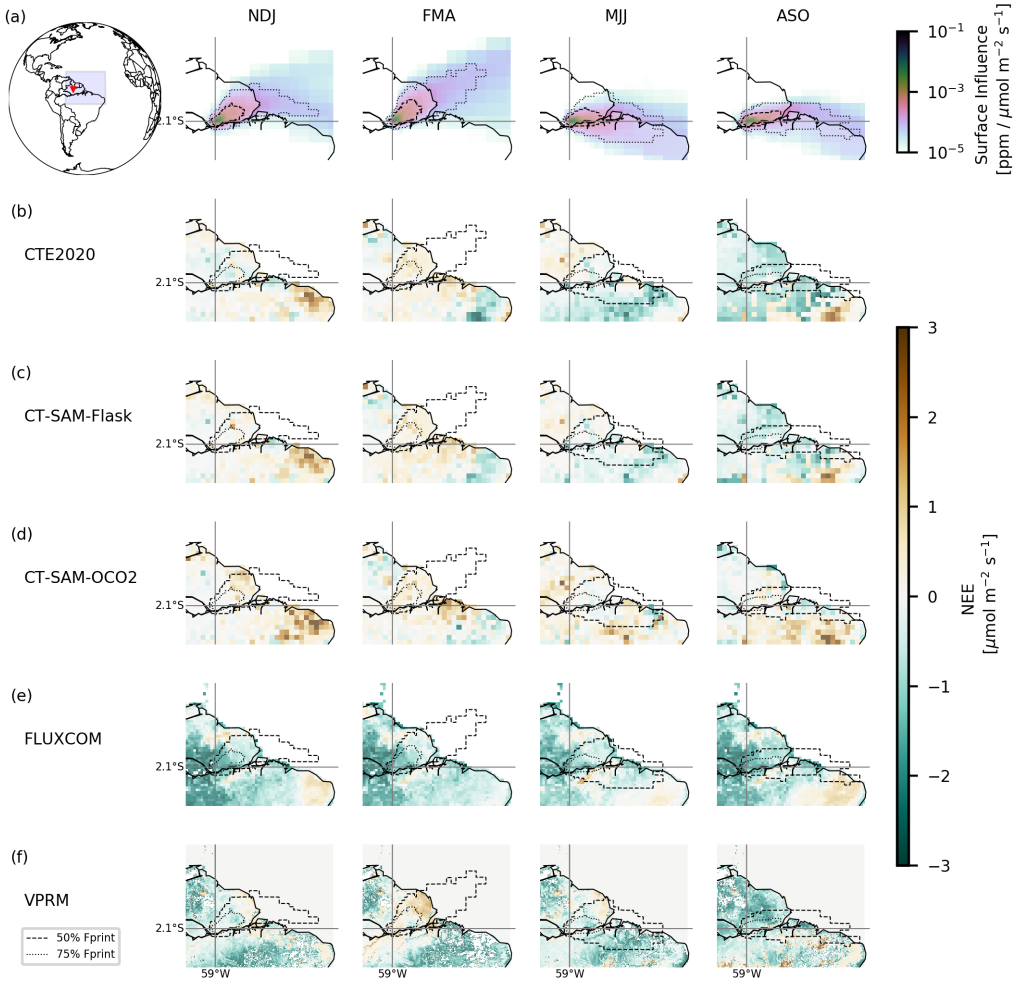

gcb_15905_f5.png

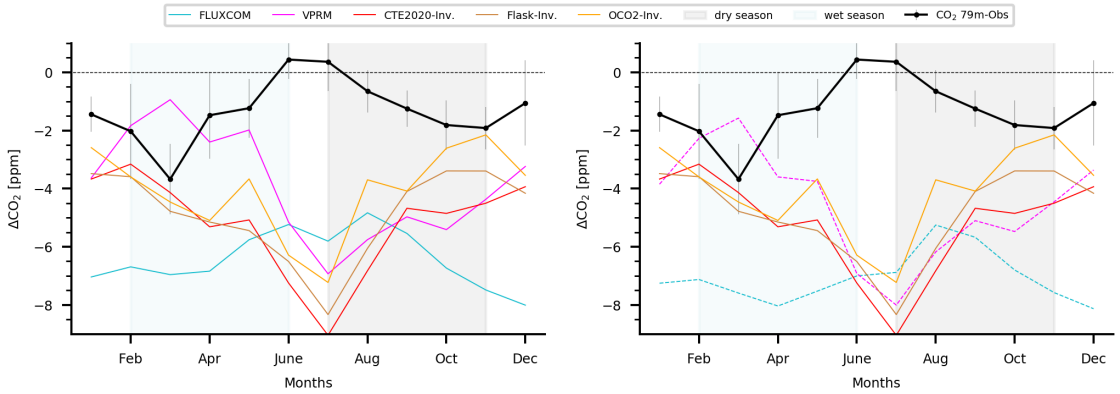

gcb_15905_f6.png

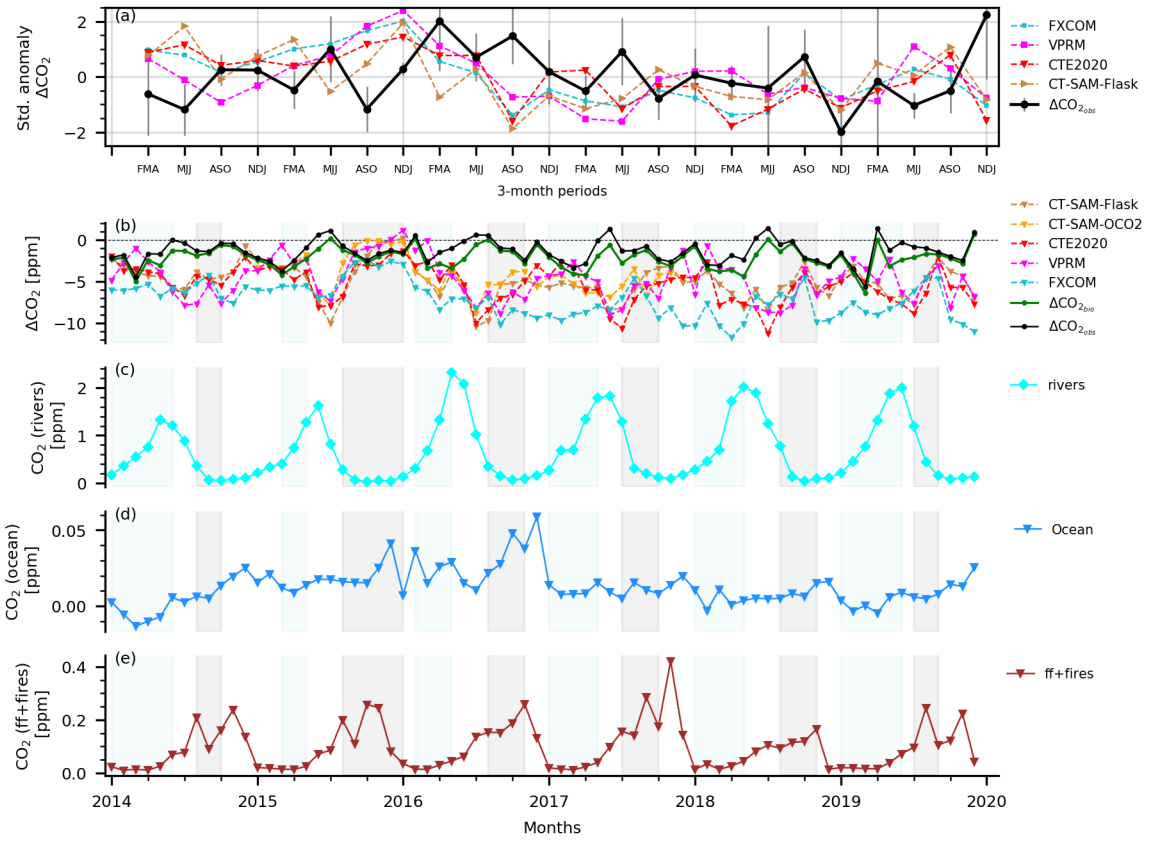

gcb_15905_f7.png

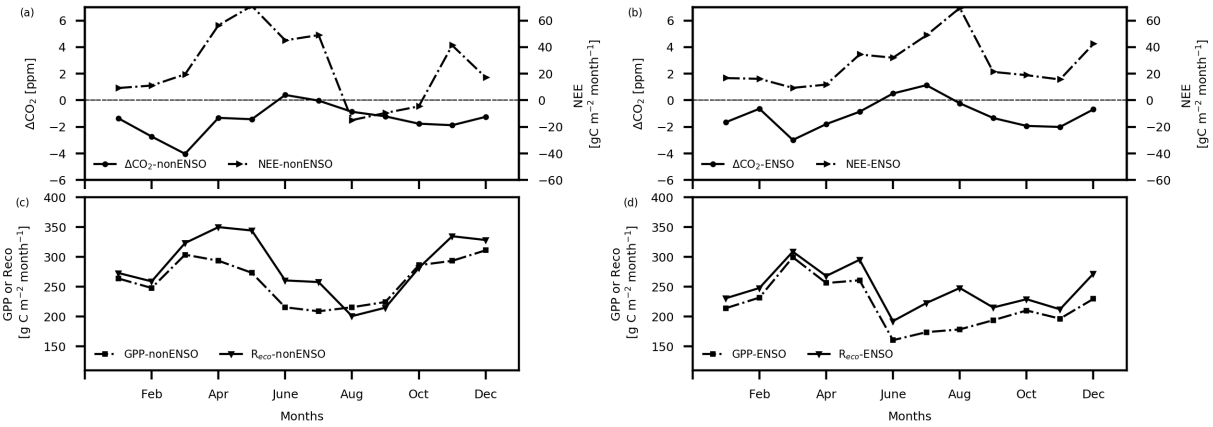

gcb_15905_f8.png